Charge distributions of Ra recoil ions produced in ^{12}C + Pb fusion-evaporation reactions

R. N. Sagaidak,[1,*] N. A. Kondratiev,[1,†] L. Corradi,[2] E. Fioretto,[2] T. Mijatovic,[3] G. Montagnoli,[4] F. Scarlassara,[4] A. M. Stefanini,[2] and S. Szilner[3]

[1]*Flerov Laboratory of Nuclear Reactions, Joint Institute for Nuclear Research, RU-141980 Dubna, Russia*

[2]*INFN, Laboratori Nazionali di Legnaro, I-35020 Legnaro (Padova), Italy*

[3]*Ruder Bošković Institute, HR-10002 Zagreb, Croatia*

[4]*Dipartimento di Fisica e Astronomia, Universitá di Padova, and INFN, Sez. di Padova, I-35131 Padova, Italy*

(Received 13 March 2018; published 31 May 2018)

Charge state distributions of the Ra recoil ions produced in the ^{12}C + Pb fusion-evaporation reactions have been obtained by measuring their yields as a function of the high voltage applied to an electrostatic deflector. Well-defined two-humped yield curves for evaporation residues (ERs) were observed. Such observations can be explained by the different sets of charge states inherent in Ra recoil ions. These charge sets correspond to the equilibrated and nonequilibrated components, as earlier observed for evaporation residues produced in different reactions. The main parameters of the distributions (mean charge values, widths, and relative intensities) for both components have been estimated using Monte Carlo simulations of the transmission of the Ra recoil ions through the deflector. For the equilibrated component the values of the mean charge and width are close to those given by different empirical systematics. For the nonequilibrated component these parameters have been obtained for the first time. The additional nonequilibrated ionization is presumably due to the formation of inner shell vacancies produced by the internal conversion of nuclear isomeric transitions of ERs. Nonequilibrated charge parameters obtained for Ra recoil ions are compared to similar available experimental data and some theoretical predictions.

DOI: 10.1103/PhysRevC.97.054622

I. INTRODUCTION

Charge state distributions of heavy ions emerging from a solid target have been studied for a long time (see, for example, reviews [1,2]). The charge states of an energetic heavy ion (HI) moving inside matter are mainly determined by the balance between the electron capture and loss in the medium. Complications in the description of charge-exchange processes are connected with the effect of multielectron losses, the appearance of metastable excited states, Auger and radiative transitions in the excited multielectron system of HIs. Such complexity is a reason why a large body of the collected experimental data exists along with a lack of reliable theoretical models. A number of empirical formulas (mainly for the mean charge Q_m and standard deviation σ_Q) was proposed to make up this deficiency (see, for example, Refs. [3–9]). Note that despite the large number of fitted parameters in the latest formulas [7–9]) and their complexity, they reproduce the observed distributions approximately, with an accuracy inadequate sometimes to a practical necessity. Moreover, in contrast to the first (semiempirical) formulas based on the Thomas-Fermi theory and Bohr's criterion [1,3], the latest ones have no physical grounds, being only based on a fit to the available experimental data.

The examples of the application of a Gaussian approximation with the Q_m and σ_Q given by some empirical formulas to the equilibrated charge state distribution for the 18-MeV ^{153}Dy evaporation residues (ERs) produced in the ^{138}Ba(^{22}Ne,7n) fusion-evaporation reaction and passed through a thin carbon foil (usually used for the equilibration of the charge distribution) [10] is shown in Fig. 1(a). As we see in the figure, all the predictions [3,4,7–9] are narrower than the experimental ones [10] along with some shifts of the mean charge values. Evidently, a Gaussian cannot describe the asymmetric distributions which are observed with very slow (when $Q_m \to 0$) or very fast (when $Q_m \to Z_{HI}$) HIs, as stressed in a number of works (see, for example, [4,5]). Note that a log-normal distribution (see below) provides a better fit to the experimental data as shown in Fig. 1(a).

So the predictive power of the empirical formulas [3,4,7–9] for the equilibrated charges is not quite good for ERs downstream the carbon foil which should equilibrate (normalize) the distributions for ERs emerging from the targets. At the same time, the charge distributions for ERs emerging directly from the targets differ dramatically from the equilibrated ones. Excited nuclear states strongly affect the ionization of inner atomic shells owing to the conversion of nuclear transitions in ERs (see [2] and references therein). Vacancies formed in the conversion of inner shells of ionized ER atoms lead to the Auger cascades which significantly increase the HI charges over the expected equilibrium magnitudes. This leads to the asymmetric charge state distributions shifted to the higher values with respect to the equilibrated ones.

For the first time such asymmetric charge state distributions were observed for rare-earth ERs as early as 1963 [11]. Afterwards very broad charge state distributions with high

*sagaidak@jinr.ru

†Deceased.

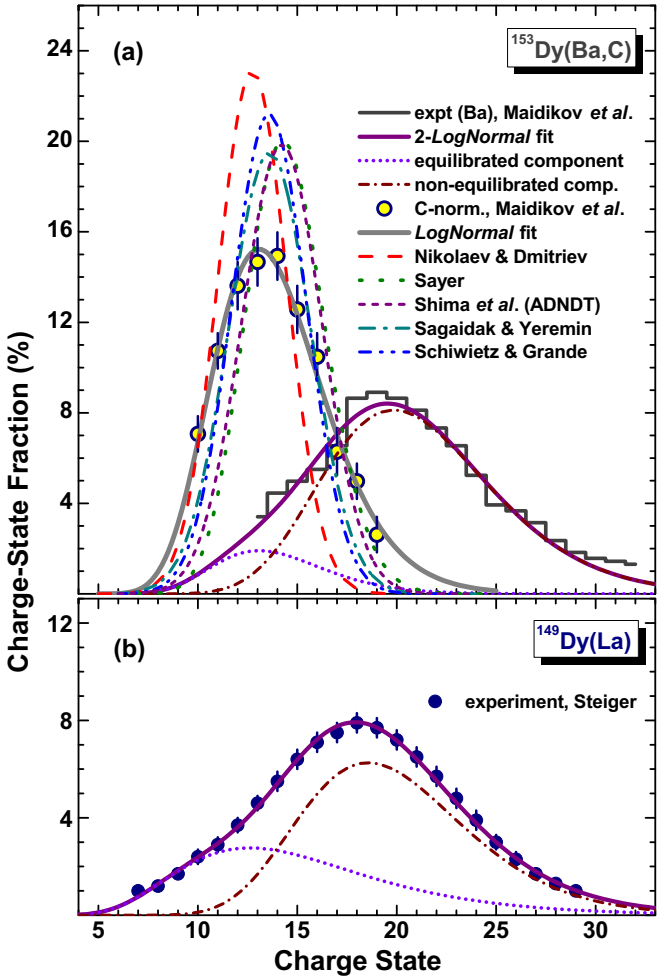

FIG. 1. (a) Measured charge state distribution of ^{153}Dy ERs produced in the fusion-evaporation reaction and emerging from the target (histogram) and observed after a carbon reset foil (open circles) as compared to Gaussian approximations according to the parametrization [3,4,7–9] (five different lines of corresponding colors). (b) Charge state distribution of ^{149}Dy ERs emerging from a La target (full circles) [11]. In both panels, one- or two-component fits to the data are shown, as obtained with log-normal functions (thick solid lines). For the two-component fits the equilibrated and nonequilibrated components are shown by dotted violet lines and by brown dash-dotted lines, respectively.

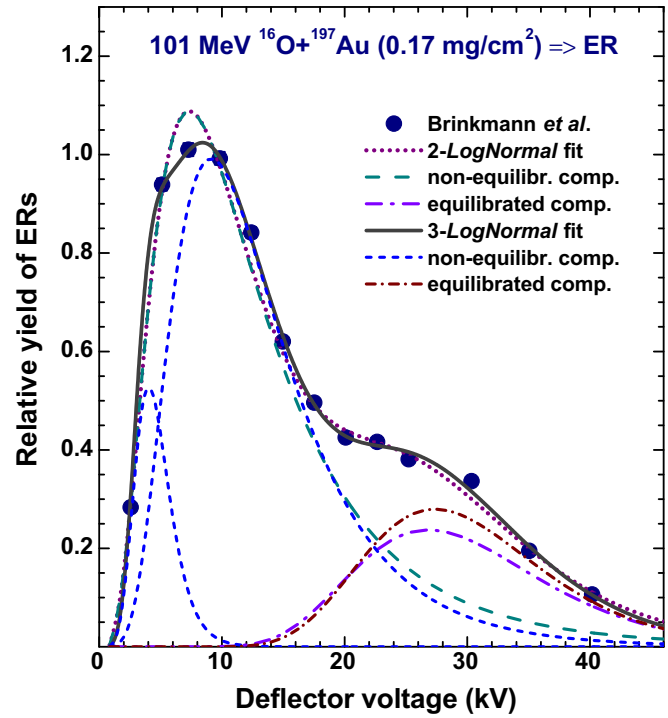

FIG. 2. The yield of ERs produced in the ^{16}O + ^{197}Au reaction as a function of a high voltage applied to the deflector [18] (full circles). Our fits to the data with the two- and three-component log-normal function, corresponding to the two- and three-component charge distributions are shown by dotted line and solid line, respectively. The decomposition of both fits is also shown by dash-dotted and dashed lines for the equilibrated and nonequilibrated components, respectively.

mean charges were observed for heavy recoil atoms produced in α decays [12,13]. Very broad charge state distributions were also observed for the recoils of transuranium nuclei produced in the (α,xn) reactions [14], and later for Dy, Pb, and Po ERs produced in (HI,xn) reactions [10,15,16]. Note that the earlier data [11], as well as the later ones [10,15,16] obtained with magnetic spectrographs, do not reveal any division between the equilibrated and nonequilibrated components for Tb-Ho, Pb, and Po ERs similarly to those shown in Fig. 1 for Dy ERs. At the same time, for relatively light and fast reaction products with masses $A \sim 60$ only the equilibrated component is clearly observed [10,16]. For heavy ERs the equilibrated component becomes clearly observable again, after passing a thin carbon foil of a sufficient thickness, installed at some distance from a target. This foil (a plunger) resets the charge state distribution to the equilibrated (normal) one [10,16], as shown in Fig. 1(a). In [16] some systematics of the mean charges of reaction products was proposed. It demonstrates a fast growth of the mean charge value with the velocity of ERs.

In practice, high charge states ($Q^+ > 15$) of ERs produced in the fusion-evaporation reactions allow one to achieve rather good separation of ERs with an electric field [17]. Thus in the study of the ^{16}O + ^{197}Au,^{208}Pb fusion-evaporation reactions two components of the charge state distributions of ERs were clearly observed with an electrostatic deflector, measuring the yield of ERs as a function of the applied voltage [18]. In fact, the curves presented in [18] allow one to extract three charge components (two of them correspond to the nonequilibrated charges and the rest to the equilibrated one). This decomposition is best done with the three-component log-normal function. A similar, but much worse description was obtained in [18] using one Gaussian for the equilibrated charges and two Gaussians for the nonequilibrated ones (see Fig. 2).

In the simulation of the ER transmission through the deflectors [17,18] extrapolations of the mean charges obtained as the result of a sudden vacancy in the K, L, and M shells for rare gases were used to obtain the corresponding functions of the atomic number [19]. There are two main approaches

in the calculation of the vacancy cascades and corresponding charge distributions following inner-shell vacancy production in atoms. The first one is based on the straightforward construction of the deexcitation decay trees for radiative and nonradiative transitions. The second approach uses the simulation of all possible radiative and nonradiative pathways to fill the inner-shell vacancies in atoms. A brief consideration of these methods and corresponding references can be found in [20], where the HI charge distributions produced after K-shell ionization are calculated using a Monte Carlo (MC) simulation.

In our study of the fusion-evaporation reactions ^{204,206,208}Pb(^{12}C,xn) [21] and ^{197}Au(^{18}O,xn) [22], leading to the production of Ra and Fr isotopes, respectively, an electrostatic deflector [23] was used to separate ERs from fission fragments, transfer reaction products, and scattered particles accompanying the reactions under investigation. A maximal yield for Ra ERs was observed at high voltage values relating to the region corresponding to the mean equilibrated charges estimated with the different systematics [3,4,6,8,9]. A similar maximum yield for Fr ERs was observed at the high voltage value which is two to three times lower than the values expected from the same systematics. Such difference could be uniquely explained by the different sets of charge states inherent in the Ra and Fr recoil ions emerging from the Pb and Au target, respectively. A more detailed experimental study of these observations was performed later [24], when a two-humped character of the yield curves for Ra and Fr isotopes produced in the corresponding reactions was revealed.

In the present work, the data on Ra and Fr charge state distributions [24] are supplemented by new ones obtained recently [25]. These data and their preliminary analysis [24,25] were published briefly in the Annual Reports of Laboratori Nazionali di Legnaro. In the present paper they are described and analyzed in more detail. The aim of the present work is an attempt to systemize main parameters of the charge state distributions for different Ra isotopes produced in fusion-evaporation reactions. These reaction products are intermediate in a mass and velocity between those considered in [10,11,15,16] and [14]. Such systematical study may initiate the development of models describing variations of charge states of ionized atoms of ERs produced in fusion-evaporation reactions, otherwise it could be useful in fusion-evaporation experiments with electromagnetic separators. For the latter, the ionic charge distributions of the recoil products determine functional properties of such devices.

In the next Sec. II we describe briefly our experiments, Sec. III is devoted to our approach to the data analysis, in Sec. IV we present our results, and in Sec. V we discuss them. Finally, in the last Sec. VI we summarize the study and make some conclusions following this work.

II. EXPERIMENT

The experiments have been performed at the XTU Tandem-ALPI accelerator complex of the Laboratori Nazionali di Legnaro of INFN. The ^{12}C and ^{18}O beams with intensities of 50–200 pnA were delivered to the targets of 150–200 μg/cm^2 thickness. The targets were placed in the center of a scattering chamber having the diameter of 100 cm. They were evaporations of the metallic ^{204,206,208}Pb on carbon backings (15 μg/cm^2) facing the beam. Isotopic enrichments of the Pb targets were higher than 97%. Detailed conditions of the experiments are presented in Table I. The beam energy losses in the carbon backings for ^{12}C and ^{18}O were taken into account in the data analysis.

TABLE I. Projectiles, laboratory-frame beam energies E_{lab}, targets, and thicknesses of targets W_T, which are used in experiments on the charge-state distribution measurements of heavy ERs.

Projectile	E_{lab} (MeV)	Target	W_T(μg/cm^2)
^{12}C	69	^{208}Pb	150
	90		
	90	^{206}Pb[a]	200
	69	^{204}Pb	150
	90		
^{18}O	90	^{197}Au[b]	150

[a]Covered with 20 μg/cm^2 carbon facing the deflector.
[b]Self-supporting metallic target.

Four silicon detectors installed inside the scattering chamber monitored continuously the beam intensity and position. They detected beam particles Rutherford-scattered from the target and were placed symmetrically above and below, to the left and right of the beam direction. The ratio of events collected in the α peaks of the α-emitting isotopes of Ra and Fr, and in the Rutherford peaks of the monitors, allowed us to obtain the yields for ERs at a given value of the high voltage applied to the deflector plates.

The forward-recoiling ERs were separated from the much higher fluxes of the beam and beamlike particles by means of the electrostatic deflector [23] installed outside the scattering chamber. The electric field generated by two pairs of metallic plates deflected the ERs into the exit diaphragm installed in front of a silicon surface-barrier detector (SSBD), while the beamlike particles with a higher electric rigidity were stopped in this diaphragm. Behind the exit diaphragm the ERs were implanted into the SSBD.

The α particle energies from the subsequent decay of the ERs were directly measured online with SSBD. Thus we could identify each isotope of Ra with mass numbers from 211 to 217 produced in the ^{12}C + Pb reactions [21,24,25]. The exception is the short-lived ^{216}Ra decaying in flight before reaching SSBD (half-life is 0.16 μs), which could not be observed. The rather long lifetime of its daughter ^{212}Rn observed in α spectra did not allow one to obtain correct yields in our online measurements. ^{211}Ra and ^{212}Ra produced in the ^{12}C + ^{204}Pb reaction at the beam energy of 90 MeV have very close α energies [26] that did not allow us to separate them unambiguously. In a similar case, ^{210}Fr and ^{211}Fr produced at the beam energy of 90 MeV in the ^{18}O + ^{197}Au reaction also have very close α energies [26] that did not allow us to separate them [22]. On the other hand, our calculations with the statistical model realized using the HIVAP code [27] predict rather small contributions of ^{211}Fr and ^{212}Ra (9% and 2%, respectively). In Table II α-decay properties of Ra isotopes

TABLE II. The most probable α-decay energies E_α, half-lives $T_{1/2}$ and α-decay branches b_α for Ra isotopes and for some of their daughters [26] observed in present work.

Nuclide	E_α (MeV)	$T_{1/2}$	b_α (%)
^{210}Fr	6.545	3.18 m	71.0
^{211}Ra	6.909	13.0 s	>93.0
^{212}Ra	6.899	13.0 s	85.0
^{213}Ra	6.522	2.73 m	80.0
	6.625		
	6.732		
^{214}Ra	7.137	2.46 s	99.94
^{215}Ra	8.700	1.55 ms	100.0
^{212}Rn	6.264	23.2 m	100.0
^{217}Ra	8.992	1.6 μs	100.0
^{213}Rn	8.089	19.5 ms	100.0

and some of their daughters observed in the present work are listed [26].

In Fig. 3 we show several examples of α spectra collected in a course of our measurements using different Pb targets and beam energies. As one can see all Ra isotopes obtained in the present work can be unambiguously identified according to their specific α-particle energies observed in the obtained α spectra. Correctness of the identification is supported by the presence of the Rn daughters indicated in the α spectra according to their α-particle energy. The detection of the ^{217}Ra recoils produced in the ^{208}Pb(^{12}C,3n) reaction at the beam energy of 69 MeV has some peculiarities. The calculated energy of the recoils (3.71 MeV) is much higher than the threshold of the detection. Due to the pulse-height defect and energy losses, these recoils can be observed in α spectra as a bump with energies lower than the calculated one. The average time of flight of ERs through the deflector is about 1.2 μs. So, due to the lifetime (see Table II) about a half of the ^{217}Ra recoils decays in flight. Some recoils implanted into the SSBD could be detected in pileups with α particles of ^{217}Ra giving the events with $E_\alpha > 8.992$ MeV in α spectra. Only a small part of ^{217}Ra, decaying at the time greater than a shaping time of our spectrometric system (1.5 μs), could be recorded with the full α-particle energy. As the result, counting rates of ^{217}Ra observed in the experiments were much less than those for ^{213}Rn, independently of the way(s) of the ^{213}Rn production (see below). Nevertheless, the events corresponding to the ^{217}Ra α decay could be extracted from the collected α spectra in most of the runs.

ERs produced in the complete fusion reactions are focused close to the beam direction and have a definite mean kinetic energy which can be determined by a straightforward calculation. The energy spread of ERs due to the evaporation of neutrons and multiple scattering can be estimated and taken into account quite definitely (see below). So the high voltage scanning in the deflector corresponds to the scanning of the charge state distribution of ERs knocked out from the target. Indeed, let $P(Q)$ be the probability density for a charge-state Q. The applied high voltage (potential difference) is proportional to the electric rigidity E_{ER}/Q, i.e., $U = kE_{ER}/Q$ (k is a constant, E_{ER} is the ER energy). With the probability densities $P(Q) = dN/dQ$ and $P(U) = dN/dU = Q^2P(Q)/(kE_{ER})$ we come to $P(U) \sim Q^2P(Q)$.

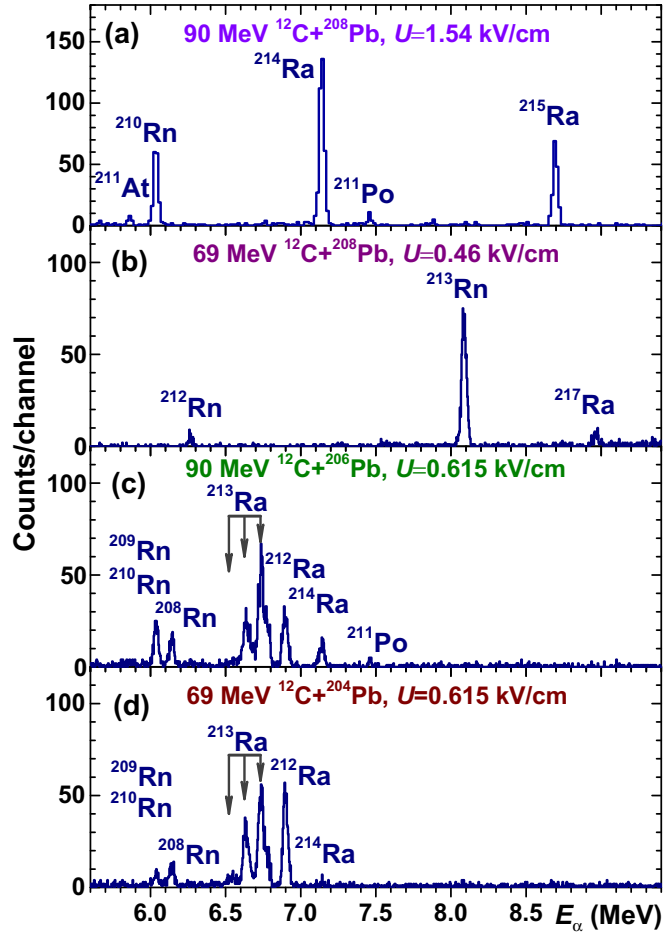

FIG. 3. Several examples of α-spectra collected in our measurements using ^{208}Pb target at the 90- and 69-MeV beam energy, panels (a) and (b), respectively; ^{206}Pb target at the 90 MeV beam energy, panel (c); and ^{204}Pb target at the 69-MeV beam energy, panel (d). Ra isotopes and their daughters identified according to the α-particle energies are indicated.

The transmission efficiency of the ERs is obtained experimentally by the ratio of the yield with a given field and the yield with no applied voltage. A total transmission has to take into account the solid angle subtended by SSBD ($\Delta\Omega \simeq 2.1 \times 10^{-5}$ sr). The transmission efficiency values were obtained for ^{214,215}Ra and ^{210}Fr in the reactions induced by ^{12}C and ^{18}O. The angular distributions for ERs could be also measured by rotating the deflector around the target position. These measurements allowed us to obtain an estimate of the energy spread of ERs in our experiments bearing in mind the interconnection of the evaporative component into of the energy and angular spreads of ERs (see, for example, [17] and below).

The yield/transmission curves were measured for ERs produced in the reactions listed in Table III. The essential characteristics for ERs escaping the targets are shown in the table. They are as follows: (1) a reaction product (ER) identified by the measured α-decay energy; (2) the average ER kinetic

TABLE III. The list of fusion-evaporation reactions used in the present study for the production of ERs and subsequent analysis of their ionic charge distributions. The ER reaction products are indicated according to their α energy detected by SSBD. A mean ER kinetic energy E_{ER} and corresponding relative velocity V/V_0 are also indicated. The main parameters of the *equilibrated* charge state distribution, such as the mean charge Q_m^{eq} and standard deviation σ_Q^{eq} predicted by the different systematics specified as ND68 [3], S77 [4], SIM82 [6], SY94 [8], SG01 [9], respectively, are listed in the same order.

Reaction	ER	E_{ER}		ND68		S77		SIM82	SY94		SG01	
	^AZ	(MeV)	V/V_0	Q_m^{eq}	σ_Q^{eq}	Q_m^{eq}	σ_Q^{eq}	Q_m^{eq}	Q_m^{eq}	σ_Q^{eq}	Q_m^{eq}	σ_Q^{eq}
$^{12}C + ^{208}Pb$	^{213}Rn	3.64	0.830	5.81	1.20	6.47	1.78	6.66	4.46	1.41	5.80	1.96
	^{217}Ra	3.71	0.830	5.88	1.21	6.54	1.80	6.75	4.61	1.43	5.87	1.99
	^{214}Ra	4.77	0.948	6.71	1.29	7.59	1.86	7.63	5.42	1.53	6.82	2.06
	^{215}Ra	4.79	0.948	6.71	1.29	7.59	1.86	7.63	5.42	1.53	6.82	2.06
$^{12}C + ^{206}Pb$	^{212}Ra	4.81	0.957	6.77	1.29	7.67	1.86	7.69	5.48	1.53	6.89	2.06
	^{213}Ra	4.83	0.957	6.77	1.29	7.67	1.86	7.69	5.48	1.53	6.89	2.06
	^{214}Ra	4.86	0.957	6.77	1.29	7.67	1.86	7.69	5.48	1.53	6.89	2.06
$^{12}C + ^{204}Pb$	^{212}Ra	3.76	0.845	5.99	1.22	6.68	1.80	6.86	4.71	1.44	5.99	2.00
	^{213}Ra	3.77	0.845	5.99	1.22	6.68	1.80	6.86	4.71	1.44	5.99	2.00
	^{211}Ra[a]	4.88	0.966	6.83	1.30	7.74	1.87	7.76	5.55	1.54	6.96	2.07
$^{18}O + ^{197}Au$	^{210}Fr[b]	7.37	1.19	8.32	1.43	9.57	1.96	9.32	7.05	1.70	8.66	2.14

[a]At a projectile energy of 90 MeV (see Table I) mostly ^{211}Ra is produced (the contribution of ^{212}Ra is estimated at about 2%) [27].
[b]The projectile energy of 90 MeV (see Table I) corresponds to the maximum of the ^{210}Fr production (the contribution of ^{211}Fr is estimated as about 9%) [27].

energy calculated as $E_{ER} = E_p A_p A_{ER}/A_{CN}^2$ (after taking into account small projectile energy losses in the carbon backing and in a half thickness of the target), where the indices p and CN denote a projectile and compound nucleus, respectively; (3) the relative velocity of the ER atom V/V_0 in units of the Bohr velocity ($V_0 = 2.188 \times 10^8$ cm/c); (4) the main parameters of the *equilibrated* charge distribution, such as a mean charge Q_m^{eq} and standard deviation σ_Q^{eq}, according to different systematics [3,4,6,8,9]. The results of the yield curve (transmission) measurements for the ERs listed in Table III are presented in Sec. IV after the data analysis outlined in the next Sec. III.

III. DATA ANALYSIS

A. Decomposition of distribution with data fit

Most of the experimental charge state distributions can be decomposed into an equilibrium and a nonequilibrium component using the log-normal function

$$\text{logn}(x) = A/(\sqrt{2\pi}\,wx)\exp\{-[\ln(x/x_m)]^2/(2w^2)\}, \quad (1)$$

where x is a charge value Q^+ in the case of the analysis of the charge distribution, or a strength of the electric field U between the deflector plates (in kV/cm) in the analysis of the yield (transmission) curve. Similar notations relate to the most probable value x_m and relative width w. Examples of the decomposition of the charge state distributions in the reactions leading to Dy ERs [10,11] are shown in Fig. 1. In Fig. 1(a) we show the one-component fit to the equilibrated charge distribution obtained with a carbon foil used for the charge equilibration (normalization) [10]. The parameter values obtained with this fit were used to decompose the charge distribution measured without the carbon foil, as shown in the same panel. In Fig. 1(b) the results of the independent two-component free-parameter fit to the data [11] are shown. This fit gives very similar parameter values for both components (the equilibrated and nonequilibrated) as compared to those obtained in the case shown in Fig. 1(a). In Fig. 2 we show an example of such decomposition for the ER yield measured as a function of a high voltage applied to the deflector used in the $^{16}O + ^{197}Au$ reaction study [18]. As one can see, the components of the yield curve can be extracted with the three-component log-normal function fit. One of them, at the highest voltages, corresponds to the equilibrated (relatively low) charges, whereas two other ones, at lower voltages, correspond to the nonequilibrated (relatively high) ones. Note that the three-component fit describes better the yield curve than the two-component one, as one can see in the figure.

In Fig. 4(a) we show the example of the similar decomposition using the two-component log-normal function fit to the transmission curve obtained for ^{210}Fr produced in the ^{197}Au(^{18}O,5n) reaction at the beam energy of 90 MeV [24,28] (see Tables I and III). As one can see in the figure, a similar shape of the transmission curve can be obtained with the MC simulation (see below) for the ^{210}Fr recoil ions [Fig. 4(b)]. The three-component charge distribution with the parameter values adjusted in this simulation [28] were used for a better description of the two-humped transmission curve obtained in the experiment [24].

One can get piecewise analytical expressions for the ion trajectories inside and outside the deflector using some simplifications. A transcendental equation for the charge of the ER ion Q^+ can be derived, neglecting some small values:

$$Q^+ = \frac{E_{ER}}{UL^2}\left[2L\tan\vartheta_0 - \Delta y - D\tan\left(\frac{Q^+UL}{E_{ER}}\right)\right], \quad (2)$$

where U is the strength of the electric field between the deflector's plates (in kV/cm) L is the effective length of the deflector's plates (in cm), Δy is the transverse displacement of

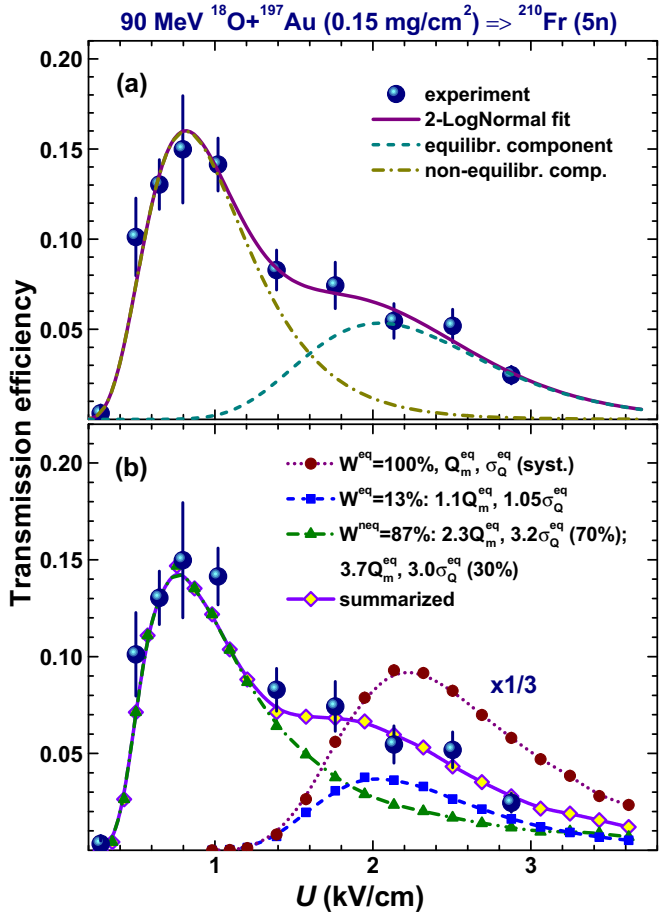

FIG. 4. The measured transmission efficiency for ^{210}Fr produced in the ^{197}Au(^{18}O,5n) reaction as a function of the electric field strength [24,28] (large filled circles with error bars). (a) Results of the two-component log-normal function fit to the measurements are shown by solid line with the decomposition into the equilibrated and nonequilibrated components (dashed and dash-dotted lines, respectively). (b) Results of the simulation using the equilibrated charges only and three-component charge distribution [28] with the mean values and standard deviations expressed through those for the equilibrated charge $Q_{\rm m}^{\rm eq}$ and $\sigma_{\rm Q}^{\rm eq}$ [8] are shown by different lines with small symbols. The indicated parameter values were adjusted to reproduce the measurements.

a central trajectory (in the electric field direction) ending at the SSBD plane with respect to its starting point at the target (in cm), ϑ_0 is the tilt of the deflector's plates with respect to the beam axis [23], D is a distance between the edge of the second deflector plates and SSBD (in cm), and $E_{\rm ER}$ is the ER energy in keV.

Equation (2) could be used at least for the estimates of the most probable charges (the equilibrated and nonequilibrated ones). It is clear that an accuracy in such estimates of the charge value is determined by the transverse dimensions of an entrance diaphragm and SSBD which are both related to Δy in Eq. (2). Thus the fitted maxima in Fig. 4 correspond to the most probable values $Q_{\rm m}^{+} = 8$ for the equilibrated charges and $Q_{\rm m}^{+} = 19$ for the nonequilibrated ones. The equilibrated value is close to the one adjusted with the MC simulation, whereas the most probable nonequilibrated value is between the two obtained in the same simulation (17 and 26) [28]. Using Eq. (2), the contribution of different components in observed yield curves can be also estimated, if the yield curve is plotted as a function of the inverse value of the strength of the electric field. Indeed, since at small deflection angles $\tan(Q^{+}UL/E_{\rm ER}) \approx Q^{+}UL/E_{\rm ER}$, Eq. (2) can be rewritten as

$$Q^{+} = \frac{E_{\rm ER}(2\tan\vartheta_0 - \Delta y/L)}{UL(1 + D/L)}, \tag{3}$$

and the abscissa $1/U$ becomes proportional to the charge Q^{+} of the ion transmitted through the deflector. It is clear that the lower (equilibrated) charge states are better manifested in the dependence on U, as one can see in Fig. 4, whereas the higher (nonequilibrated) charge states become better visible in the dependence on $1/U$. In the following, we prefer to present the experimental and simulated transmissions as a function of U.

B. Simulation of the ER transmission through the deflector

According to Eq. (2), the estimate of the ER charge derived from experiments is determined by a number of parameters corresponding to both the geometry of the deflector and kinematical characteristics of ERs. The latter have their own distributions that should be taken into account in the estimates. A MC simulation for ERs transmitted through the deflector allows one to take into account a spread in the ER energy and emerging angle in Eq. (2), when the charge distribution components are adjusted to reproduce the yield (transmission) curve.

The energy and angular distributions of the ER recoils entering the deflector are determined by the evaporation of light particles from a CN, as well as by their energy loss and multiple scattering by target atoms. The last two processes are interconnected and can be considered with the MC TRIM simulation [29]. In our simulations we assumed the uniform production of ERs along the target thickness that is a good approximation for relatively thin targets giving small projectile energy losses as in the present experiments. The initial energy and angular distributions for ERs produced inside the target, which are determined by evaporation of light particles, were randomly simulated using mean energies of the evaporated particles at each step of the CN deexcitation chain leading to the observed ER. These mean energies were obtained with the statistical model calculations [27]. The statistical model [27] was successfully used earlier for the description of the ER and fission excitation functions [21,22,30]. The use of the sequential computation of the velocity vectors of heavy nuclei produced at each evaporation step allows us to take into account charged particle emission (protons and alphas) taking place at the CN deexcitation along with the emission of neutrons. This approach extended the description of the energy and angular distributions, which was earlier applied to the reactions with neutrons evaporation only [28]. As one could expect, simulations based on this extended approach were in good agreement with the measured ER angular distributions considered earlier [28].

In Fig. 5 some examples of the energy distributions obtained with the MC simulations are shown for ^{210}Fr produced in the

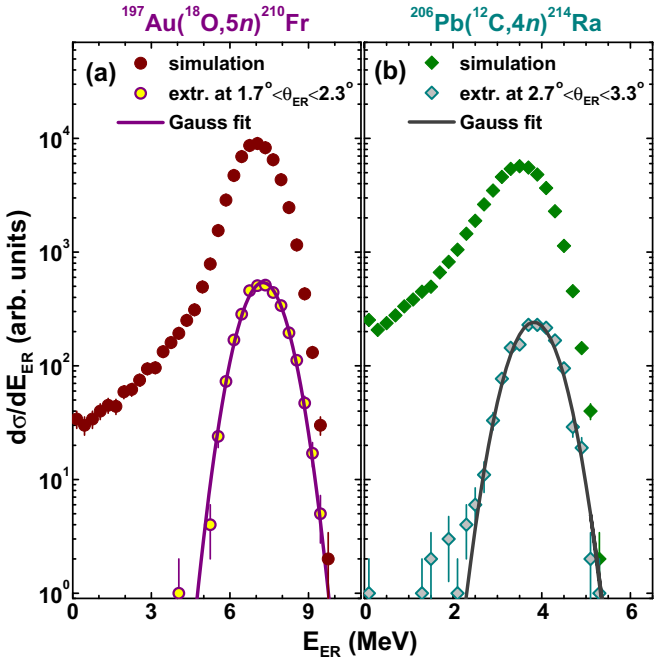

FIG. 5. The energy distributions obtained with the Monte Carlo simulations as described in the text (a) for ^{210}Fr produced in the ^{197}Au(^{18}O,5n) reaction and (b) for ^{214}Ra produced in the ^{206}Pb(^{12}C,4n) reaction (filled symbols). The energy distributions for the events extracted according to the deflector angular acceptance are shown by open symbols with the Gaussian fits to the data (solid lines).

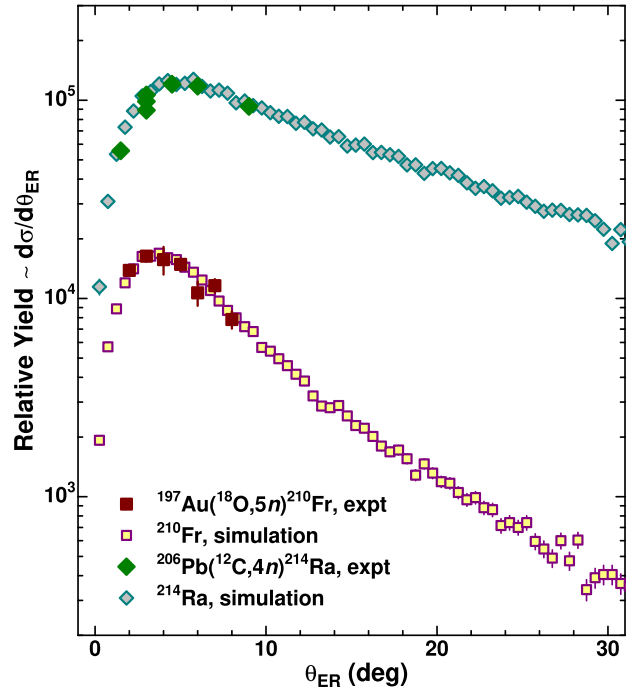

FIG. 6. The angular distributions measured for the same ERs produced in the same reaction as shown in Fig. 5 (filled symbols) in comparison with those obtained using Monte Carlo simulations (open symbols).

^{197}Au(^{18}O,5n) reaction at $E_{\rm lab} = 90$ MeV (see Tables I and III) and for ^{214}Ra produced in the ^{206}Pb(^{12}C,4n) at $E_{\rm lab} = 73$ MeV. In the last case a 200 μg/cm^2 target turned at 60° to the beam direction was used for the angular distribution measurement (see below). As one could expect, stopping inside the target has a pronounced effect on the low energy "tail" of heavy and slow ERs. The tail disappears for the events extracted from the total energy distributions in accordance with a small angular acceptance at forward angles, to which our measurements with the deflector correspond.

The results of the simulations of the energy distribution at forward angles (similar to those shown in Fig. 5) allowed us to perform trajectory calculations for ERs passing through the deflector with the use of the approximation of an "effective entrance diaphragm." This diaphragm had the same position as a true one installed at the entrance of the deflector (C_3 in Fig. 1 of Ref. [23], with a width of 20 mm). In contrast to the physical (true) diaphragm, the "effective" one, having a smaller size, provided the same angular acceptance, as it was determined by the solid angle subtended by the SSBD. With this approximation, a set of entrance trajectories is determined by the sizes of the beam spot on the target (~3 mm in diameter) and the effective diaphragm (~5 mm in a diameter) as well as a distance between them (~0.9 m). In simulations we used uniform distributions for ERs produced over the target area and for those coming into the effective diaphragm. With such approximations the ER angular distributions are not important for the simulation, whereas the ER energy distribution cut by a narrow interval of forward angles can be approximated with a Gaussian (see Fig. 5). The approximation of the "effective entrance diaphragm" allowed us to use the simulations more effectively, bearing in mind that only several percent of ERs escaping the target can pass through the entrance diaphragm (see Fig. 5). Note that a good agreement of the results of thus performed simulations with the absolute transmission efficiency measurements (see below) validates this approximation.

At the same time, as we mentioned above, the simulated angular and energy distributions are interconnected [29]. The simulated angular distributions can be easily compared to the experimental ones while the direct measurement of the ER energy distributions is questionable due to an uncertain quantity of the pulse-height defect in the SSBD. Such a comparison of the angular distributions is shown in Fig. 6.

For the trajectory calculations inside the deflector we set initially a normal charge distribution with the mean charge $Q_{\rm m}^{\rm eq}$ and standard deviation $\sigma_{\rm Q}^{\rm eq}$ estimated with the systematics for the equilibrated charges [8]. These parameters were scaled to adjust the simulated transmission (yield) curve to the measured one as indicated in Fig. 4(a). With such scaling one could reproduce the measured transmission curves using two or three sets of charge state distributions (in fact, there could be even more than three [14]), as shown in the figures. As we can see, the adjusted parameters of the first component, corresponding to the rather high electric rigidity, are very close to those obtained for the equilibrated charges [8]. The second maximum in the transmission curves correspond to the relatively low electric rigidity which is related to the nonequilibrated component. It can be reproduced, in turn, in the simulations using the two-component charge distribution

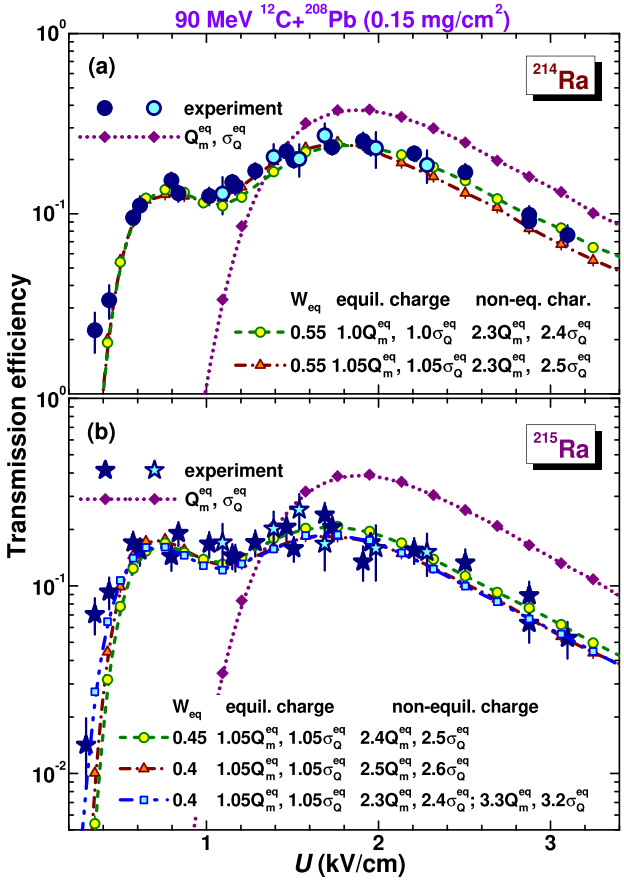

FIG. 7. Transmission efficiency curves measured (a) for ^{214}Ra and (b) for ^{215}Ra produced in the ^{208}Pb(^{12}C,6n) and ^{208}Pb(^{12}C,5n) reactions, respectively [24] (large symbols). Open symbols correspond to the yield data obtained at the studies [21] and normalized to the transmission curves. Simulations with the adjusted parameter values are shown by small open symbols connected with different lines. In the case of ^{215}Ra, the adjustment was performed with the two-component nonequilibrated charge distribution. The simulated transmission curves corresponding to the equilibrated charges [8] are also shown for the comparison (full diamonds connected by dotted lines). The relative weights of the equilibrated component W_{eq}, mean values and standard deviations of the equilibrated and nonequilibrated components are expressed with the values corresponding to the equilibrated charges Q_m^{eq} and σ_Q^{eq} [8].

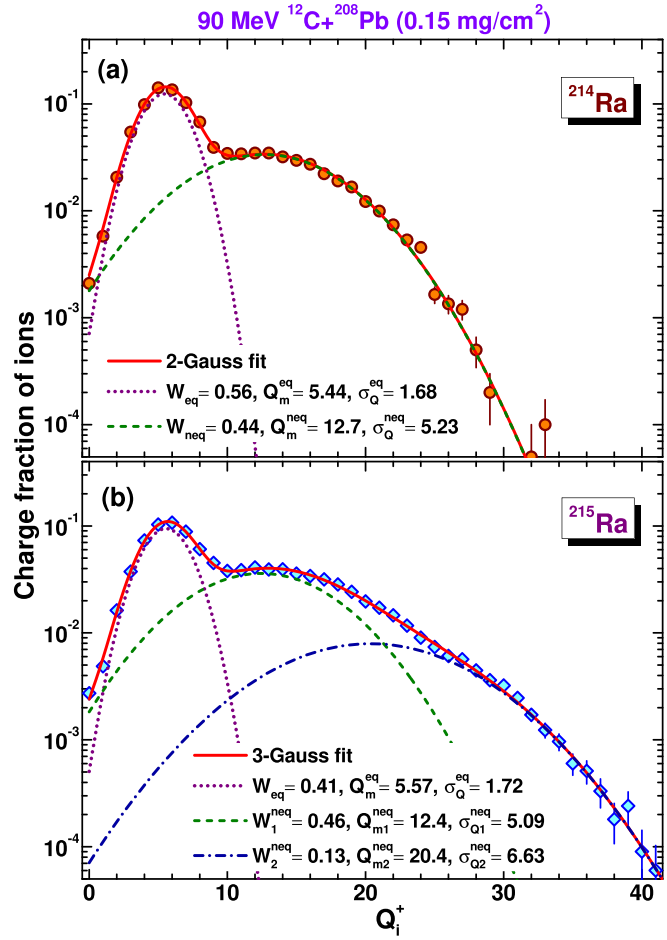

FIG. 8. Charge state distributions (a) for ^{214}Ra and (b) for ^{215}Ra, which correspond to the best adjustment of simulations to the measurements shown in Fig. 7 (open symbols). The parameter values are also indicated.

with the mean charge values higher than the equilibrated one and with the larger values of standard deviations [see Fig. 4(a)].

IV. RESULTS OF MEASUREMENTS AND SIMULATIONS

A. Charges of ER recoils produced in ^{12}C + ^{208}Pb

The transmission efficiency curves for ^{214}Ra and ^{215}Ra, which were measured as a function of the strength of the electric field U in the same runs, are shown in Fig. 7 [24]. The ERs were produced in the 6n and 5n evaporation channels at the beam energy of 90 MeV. Production of these Ra isotopes is unambiguously determined by their specific α energies (see Table II and Fig. 3). We added to these measurements the yield data obtained earlier with the thicker target (0.2 mg/cm^2) in the course of the fusion reaction studies [21]. The yield data were normalized to the observed transmission efficiency curve maxima.

As in the case shown in Fig. 5, in the transmission simulations we used the energy distributions for ^{214}Ra and ^{215}Ra, which corresponded to the Gaussian fits to their energy spectra resulting from the extraction of the ER events emitted at $\theta_{ER} = (4 \pm 0.3)^\circ$. The transmission curves shown in Fig. 7 were measured at the same angle. As we see, the transmission curves for ^{214}Ra and ^{215}Ra are distinct from each other. Namely, the yield of the nonequilibrated component corresponding to the lower strength of the electric field is higher for ^{215}Ra as compared to the one for ^{214}Ra. This visible difference is confirmed by the transmission simulations adjusted to the measured curves. The best fitted transmission curves correspond to the intensities (weights) for the equilibrated components $W_{eq} = 0.55$ and 0.4 for ^{214}Ra and ^{215}Ra, respectively. Moreover, the ^{215}Ra data imply the availability of the second nonequilibrated components with higher charges (the adjustment with $Q_m^{neq} = 3.3 Q_m^{eq}$ and $\sigma_Q^{neq} = 3.2\sigma_Q^{eq}$ better reproduces the data at low values of the electric field strength). Such results of simulation may also imply a non-Gaussian distribution of the nonequilibrated

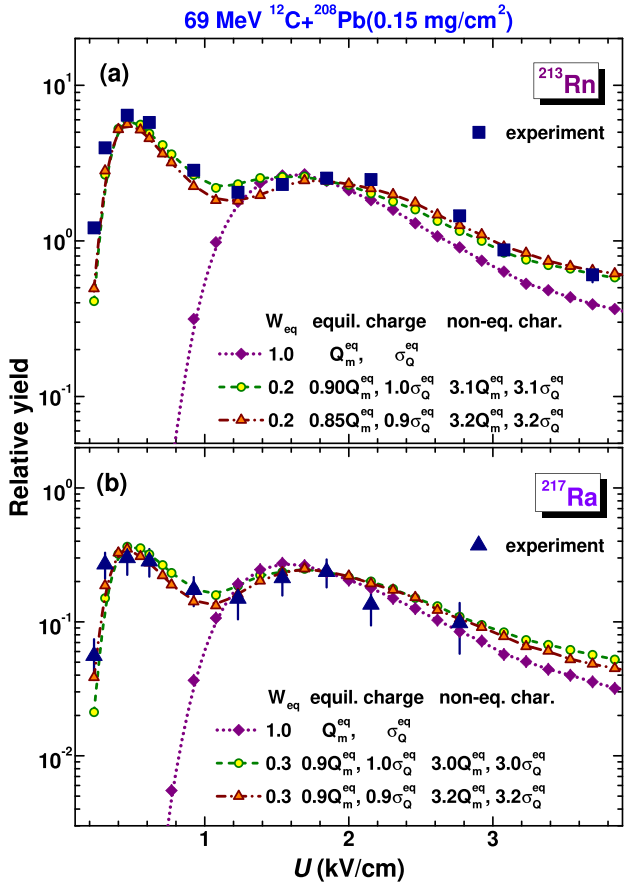

FIG. 9. The same as in Fig. 7 but (a) for the yield of ^{213}Rn and (b) for the yield of ^{217}Ra produced at the beam energy of 69 MeV. The yield curves obtained with simulations are normalized to the experimental maxima observed for the equilibrated charges at $U = 1.846$ kV/cm.

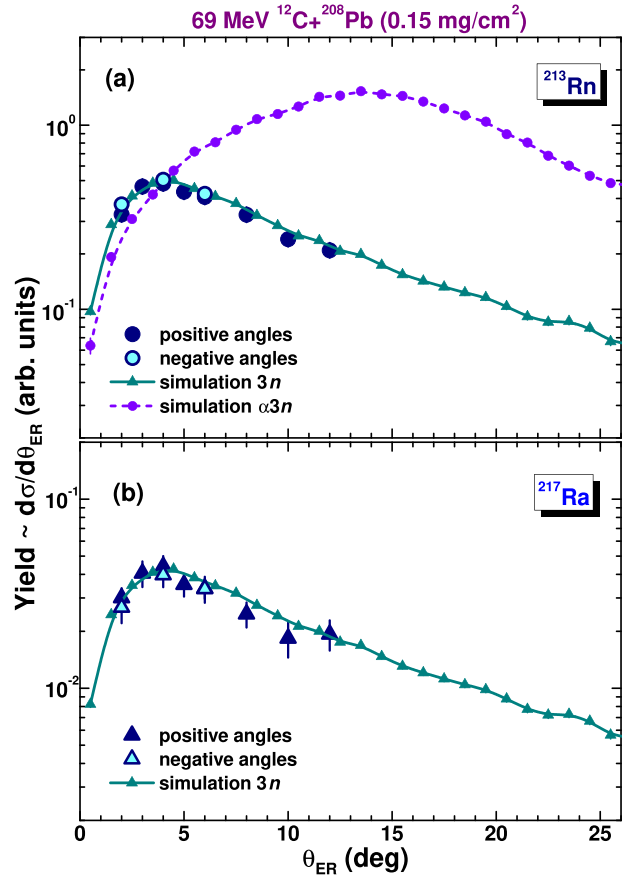

FIG. 10. The angular distributions (a) for ^{213}Rn and (b) for ^{217}Ra produced at the beam energy of 69 MeV (large symbols), as obtained in our measurements. Simulations for the 3n and α3n evaporation channels, which are normalized to the experimental maxima of the distributions, are shown by small symbols connected with the solid lines and dashed line, respectively.

component, which is reproduced by a second nonequilibrated Gaussian component shifted to higher charge states. At the same time, for the equilibrated components of ^{214}Ra and ^{215}Ra the average charge and standard deviation values are close to each other.

In Fig. 8 we show the charge state distributions for ^{214}Ra and ^{215}Ra corresponding to the best adjustment of simulations to the measured transmission curves shown in Fig. 7. As mentioned above, the two-component distribution for nonequilibrated charges better reproduces the transmission curve for ^{215}Ra at low electric field strengths. This three-component charge distribution is shown in the figure. Both sets of the simulated data are accompanied by multi-Gaussian fits with the absolute charge parameter values indicated in the figure.

We also measured the yield curves for ^{213}Rn and ^{217}Ra at $E_{lab} = 69$ MeV in our recent experiments [25], as shown in Fig. 9. Production of these ERs is unambiguously determined by their specific α energies (see Table II and Fig. 3). ^{217}Ra is the product of the 3n fusion-evaporation reaction. ^{213}Rn could be produced as the daughter of ^{217}Ra via its prompt α decay, or/and as a result of the α3n fusion-evaporation reaction, or/and as a result of the direct Be-cluster transfer to the target nucleus accompanied by the emission of the He ejectile. The presence of the two last processes was earlier observed in the ^{12}C + Bi reaction at energies well above the Coulomb barrier [31,32]. Production of ^{213}Rn is of interest to the reaction mechanism, as well as an additional ionization in-flight produced by the α-decay of its short-lived ^{217}Ra precursor.

Simulations of the yields adjusted to the data for ^{213}Rn and ^{217}Ra (see Fig. 9) showed very similar parameter values for their charge distributions, with the exception of the relative intensities (weights) of the equilibrated charge components. Some reduction in the yield for ^{213}Rn as compared to the similar one for ^{217}Ra was observed. At the same time, very close values of the charge distribution parameters may reflect the similarity in the kinematics of the corresponding reaction products.

A comparison of the angular distributions obtained for ^{213}Rn and ^{217}Ra clarifies the production way of the former. This comparison is shown in Fig. 10 for the measured distributions and simulated ones. As we can see, the simulated angular distribution for the 3n evaporation channel is very close to the measured one for both ^{213}Rn and ^{217}Ra. Clearly, the angular distribution simulated for the α3n evaporation channel leading to ^{213}Rn should be much broader with a maximum position at a

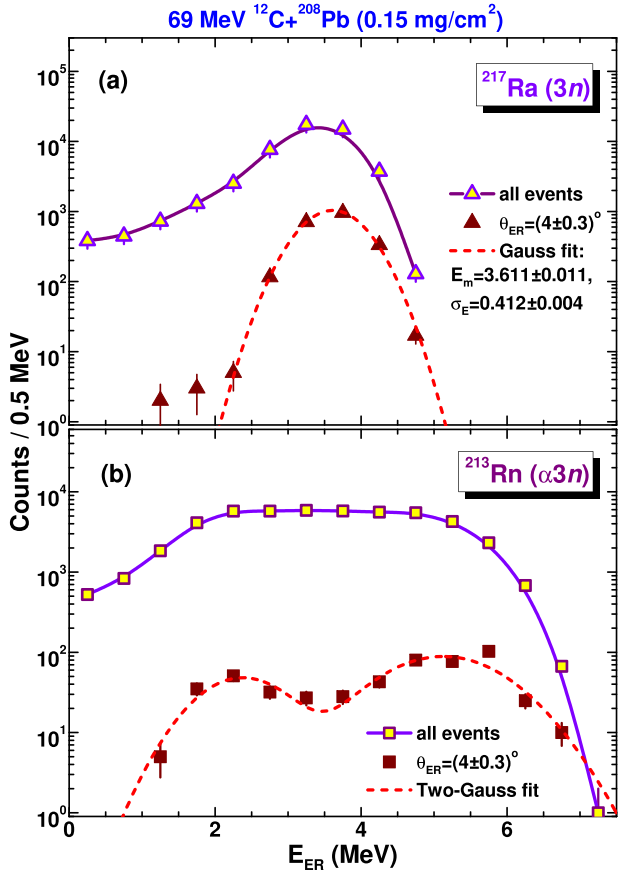

FIG. 11. The energy distributions (a) for ^{217}Ra and (b) for ^{213}Rn obtained with the simulations as the result of the 3n and α3n fusion-evaporation reactions for all ER events (open symbols connected with solid lines). The events corresponding to the angles $\theta_{ER} = (4 \pm 0.3)^\circ$ are shown by solid symbols. The results of one- and two-component Gaussian fits to these distributions are shown by dashed lines.

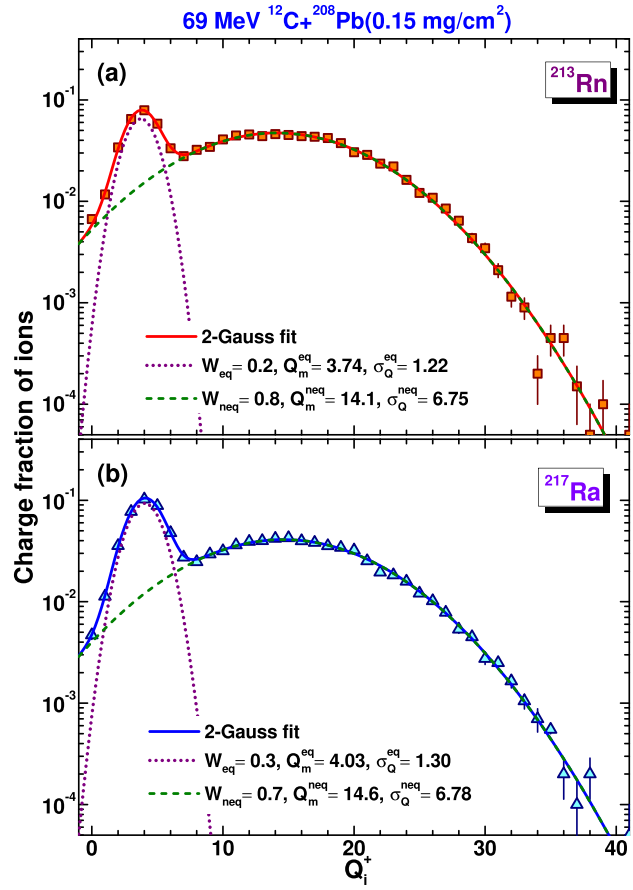

FIG. 12. The same as in Fig. 8, but (a) for the ^{213}Rn charge distribution and (b) for the ^{217}Ra charge distribution, which correspond to the best adjustments of simulations to the measurements shown in Fig. 9.

large angle as shown in Fig. 10 and in the experiments [31,32]. Thus, according to this comparison, one can state that the most of ^{213}Rn observed in our experiments comes from the α decay of ^{217}Ra, i.e., it corresponds to the 3n evaporation channel.

This statement is supported by the ER energy distributions simulated for ^{213}Rn and ^{217}Ra resulting from the α3n and 3n evaporation channels, respectively. These simulations together with the extraction of the recoil events at the forward angle $\theta_{ER} = (4 \pm 0.3)^\circ$, corresponding to the yield curve measurements (Fig. 9), demonstrate a significant difference in the energy distributions of ^{213}Rn and ^{217}Ra produced in the different evaporation channels, as shown in Fig. 11. The double-humped energy distribution for ^{213}Rn resulting from the α3n reaction is a consequence of the narrow angle selection corresponding to the α-particles emission in forward and backward directions. In principle, such distribution should give us a four-humped yield curve measured with the deflector by analogy with the one-humped energy distributions which produces the double-humped yield curves observed in our experiments. That is not the case and supports our statement that most of ^{213}Rn observed in the experiments comes from the α decay of ^{217}Ra, i.e., it corresponds to the 3n evaporation channel. The Gaussian fit to the energy distribution of the 3n-channel events extracted at $\theta_{ER} = (4 \pm 0.3)^\circ$ provides the parameter values [indicated in Fig. 11(a)] for the simulations of the ^{213}Rn and ^{217}Ra yields shown in Fig. 9.

In Fig. 12 we show the charge distributions for ^{213}Rn and ^{217}Ra, as derived with the best adjustments of simulations to the measured yield curves shown in Fig. 9. Note that the charge parameter values for their nonequilibrated components Q_m^{neq} and σ_Q^{neq} are distinctly higher than those obtained for ^{214}Ra [see Fig. 8(a)]. At the same time, in contrast to the previous case for ^{215}Ra [see Fig. 8(b)], there was no need to introduce the second nonequilibrated component with higher charges to describe the yields of ^{213}Rn and ^{217}Ra at low electric field strengths in simulations.

B. Charges of ER recoils produced in ^{12}C + ^{206}Pb

The yield curves for Ra recoils produced in the ^{206}Pb(^{12}C,xn) reactions at $E_{lab} = 90$ MeV were recently obtained in our experiments [25]. These curves for ^{213}Ra and ^{212}Ra produced in the 5n and 6n evaporation channels, respectively, are shown in Fig. 13. The yield curve for ^{214}Ra produced in the evaporation 4n channel is shown in Fig. 14. Production of these Ra isotopes is unambiguously determined by their specific α energies [see Table II and Fig. 3(c)].

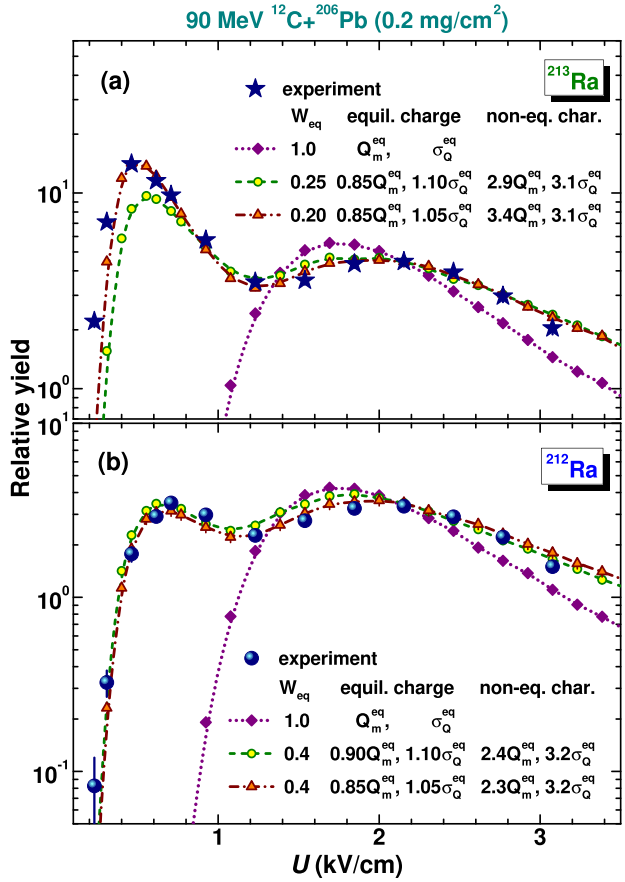

FIG. 13. The same as in Figs. 7 and 9, but (a) for the yield of ^{213}Ra and (b) for the yield of ^{212}Ra, which are produced in the $5n$ and $6n$ evaporation channels, respectively, on the ^{206}Pb target at $E_{\rm lab} = 90$ MeV. The simulated curves were normalized to the measured maximum yields corresponding to the equilibrated charges.

As in the previous cases illustrated in Figs. 5 and 11(a), we used the ER energies obtained with the MC simulations.

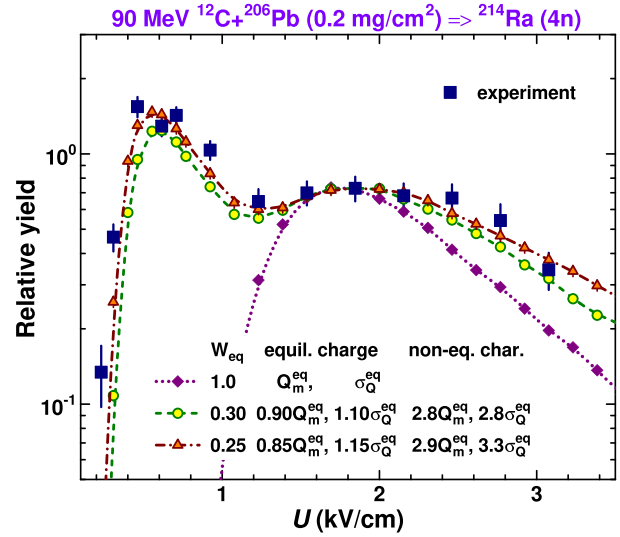

FIG. 14. The same as in Fig. 13, but for the yield of ^{214}Ra produced in the $4n$ evaporation channel.

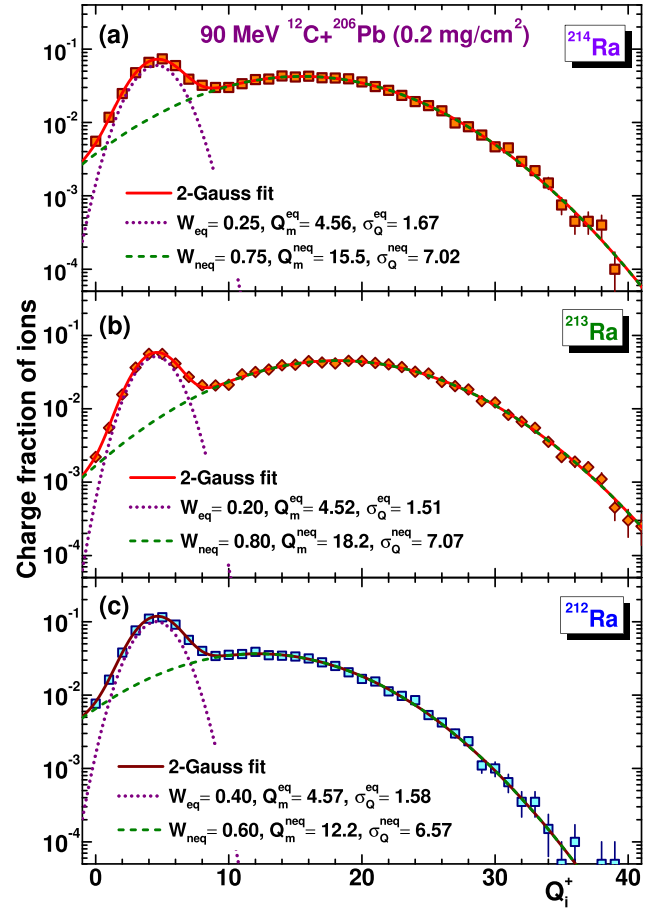

FIG. 15. The same as in Fig. 8, but (a) for the ^{214}Ra charge distribution, (b) for the ^{213}Ra charge distribution, and (c) for the ^{212}Ra charge distribution, which correspond to the best adjustments of simulations to the measurements shown in Figs. 13 and 14.

The Gaussian fits to the energy distributions resulting from the recoil events ejected at the angle of the yield measurements $\theta_{\rm ER} = (3 \pm 0.3)^\circ$ gave us the parameter values used in the yield simulations. As in the previous observations, the measured two-humped yield curves could be described with the two-component charge distributions as shown in Figs. 13 and 14. The charge distribution parameters indicated in the figures are expressed with reference to the equilibrated distributions as always. In Fig. 15 we show the charge distributions for the ^{213}Ra, ^{212}Ra, and ^{214}Ra recoil ions that best reproduce the measured yield curves obtained in the simulations.

C. Charges of ER recoils produced in ^{12}C + ^{204}Pb

In Fig. 16 we show the yields of ^{211}Ra produced in the ^{204}Pb(^{12}C,$5n$) reaction at $E_{\rm lab} = 90$ MeV as a function of the electric field strength as obtained in our earlier measurements [24]. Production of ^{211}Ra is unambiguously determined by its specific α energy. Actually, some admixture of ^{212}Ra produced in the $4n$ reaction might contribute to the observed α peak (see Table II). Such contribution is about 2% according to the statistical model calculations [27]. At the same time, assuming that the calculated cross-section ratio σ_{5n}/σ_{4n} may be lower by

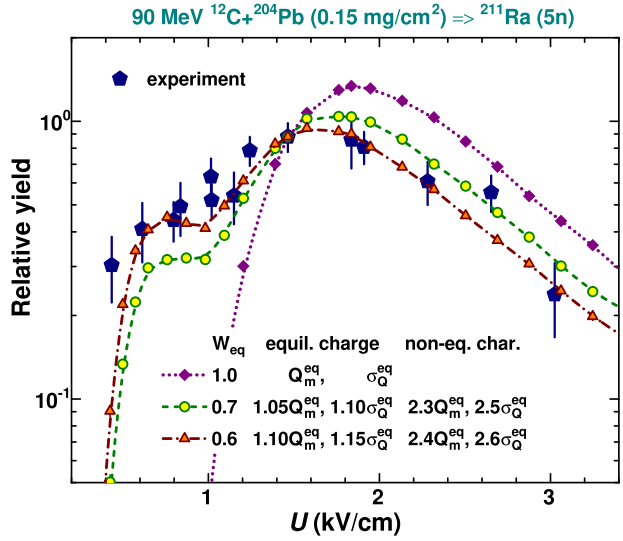

FIG. 16. The same as in Fig. 14 but for ^{211}Ra produced in the ^{204}Pb(^{12}C,5n) reaction.

a factor 2, as in the case of the same reactions taking place with the ^{206}Pb target, the contribution of ^{212}Ra should not exceed of 5%.

In the ^{12}C + ^{204}Pb study at $E_{lab} = 90$ MeV we also observed some activity assigned to ^{210}Ra ($E_\alpha = 7.016$ MeV, $T_{1/2} = 3.7$ s [26]) which can be produced in the 6n reaction. Unfortunately, production rates of ^{210}Ra were much lower than those for ^{211}Ra that did not allow us to obtain a well-defined yield curve.

In Fig. 17 we show the yield curves for ^{213}Ra and ^{212}Ra produced in the 3n and 4n evaporation channels, respectively. These curves were obtained at the beam energy $E_{lab} = 69$ MeV in our recent measurements [25]. At this energy the same Ra isotopes are produced as in the case of the evaporation reactions with the ^{206}Pb target at $E_{lab} = 90$ MeV, but the relative yields of Ra isotopes are somewhat different [see Fig. 3(d)]. Thus the low yield of ^{214}Ra produced in the 2n evaporation channel did not allow us to obtain a well-defined yield curve.

As in the previous cases, the two-humped yield curve shown in Figs. 16 and 17 could be reproduced with a two-component charge distribution. The charge distribution parameters expressed in terms of the corresponding values for the equilibrated charges are indicated in these figures. In Fig. 18 we show the charge distributions for the ^{211}Ra, ^{212}Ra, and ^{213}Ra recoil ions. The charge distribution parameters indicated in the figure are expressed with the absolute values as usual. They correspond to the best adjustments of simulations to the measured yield curves shown in Figs. 16 and 17.

D. Charges of ^{210}Fr recoils produced in ^{18}O + ^{197}Au

As we mentioned above, the angular, energy and charge distributions for ^{210}Fr produced in the ^{197}Au(^{18}O,5n) reaction were considered earlier [28] (see Figs. 11–14 therein and Figs. 5 and 6 in the present work). The transmission curve measured at $\theta_{ER} = 2^\circ$ [24] (see Fig. 4) constrains the relative contribution of the equilibrated and nonequilibrated

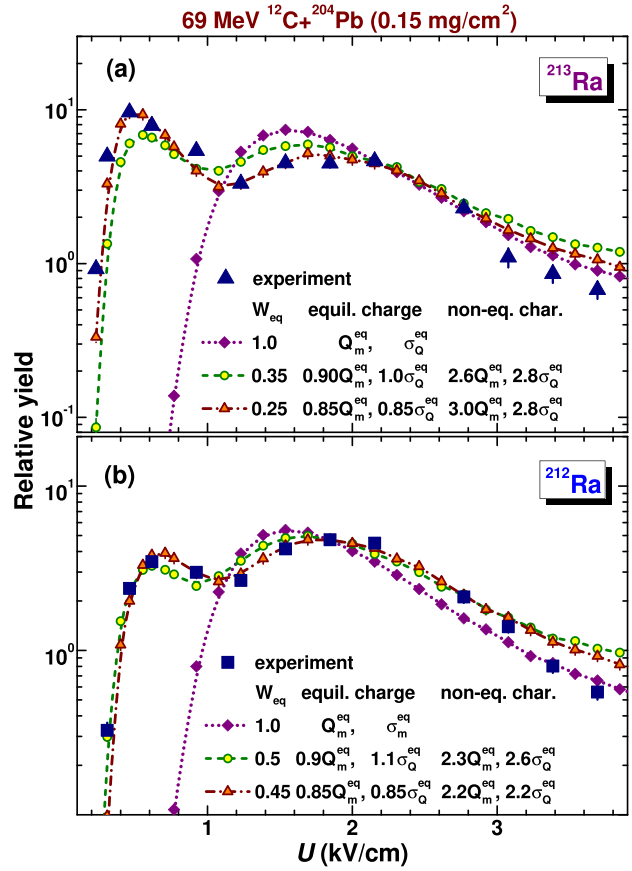

FIG. 17. The same as in Fig. 16, but (a) for the yield of ^{213}Ra and (b) for the yield of ^{212}Ra, which are produced in the 3n and 4n reactions, respectively, at the beam energy $E_{lab} = 69$ MeV.

components within $W_{eq} = 13$–16% and $W_{neq} = 87$–84%, respectively, as obtained in simulations [28]. The equilibrated component corresponds to the mean charge and standard deviation values equal to $1.1\,Q_m^{eq}$ and $1.05\sigma_Q^{eq}$, respectively. The nonequilibrated charges reveal two components with the mean charge values corresponding to 2.3–2.4$\,Q_m^{eq}$ and 3.6–3.7$\,Q_m^{eq}$ and standard deviations corresponding to 2.9–3.2σ_Q^{eq}. The relative contributions of the two nonequilibrated components with "smaller" and "larger" charges vary within $w_1^{neq} = 60$–70% and $w_2^{neq} = 40$–30%, respectively. In Fig. 19 we show the charge distribution for ^{210}Fr in the same way as shown for Ra isotopes. This distribution corresponds to the absolute charge parameter values giving the best description of the transmission curve shown in Fig. 4.

V. DISCUSSION

A. Qualitative analysis

An overview of the results of the data analysis presented in Figs. 4, 7–9, and 12–19 shows quite good agreement with the predictions of the systematics for the equilibrated charges of heavy ions [8] (maximal deviations correspond to +10% and −15% for Q_m^{eq}, and ±15% for σ_Q^{eq}). We remind that this systematics is based on charge state distributions of ions emerging from a carbon foil. In the present application the

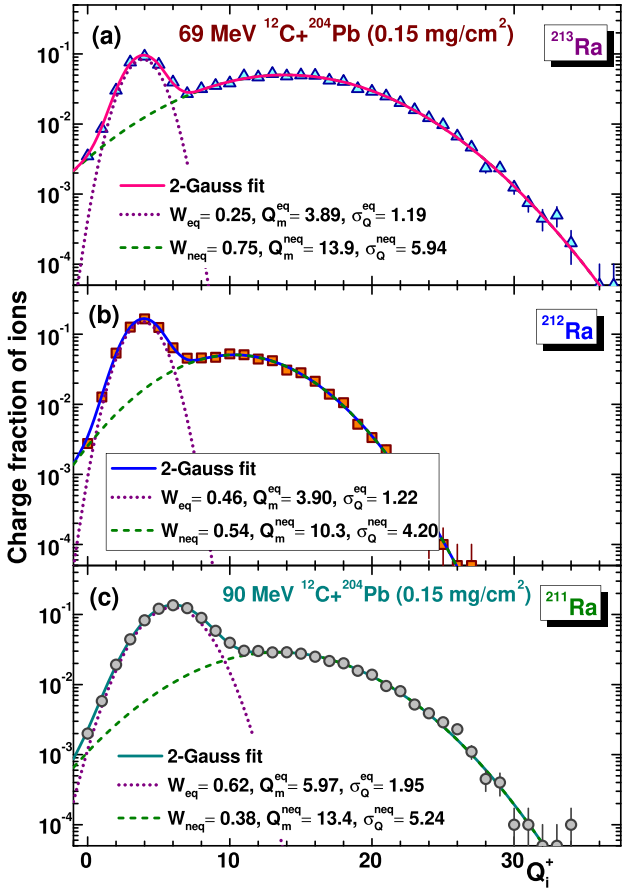

FIG. 18. The same as in Fig. 15, but (a) for the ^{213}Ra charge distribution, (b) for the ^{212}Ra charge distribution, and (c) for the ^{211}Ra charge distribution, which correspond to the best adjustments of simulations to the measurements shown in Figs. 16 and 17.

Q_m^{eq} values calculated with the systematics were scaled to the target Z with the relation proposed in [6], whereas the

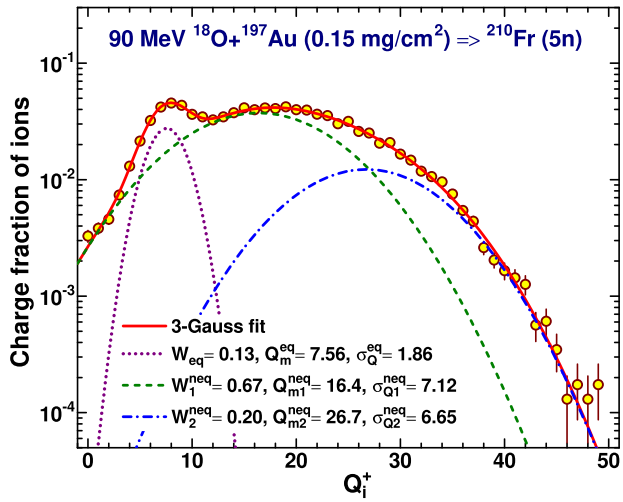

FIG. 19. The same as in Fig. 15, but for the charge distribution of ^{210}Fr produced in the ^{197}Au(^{18}O,5n) reaction at $E_{lab} = 90$ MeV. The charge parameter values correspond to the best adjustments of simulations to the measurements shown in Fig. 4.

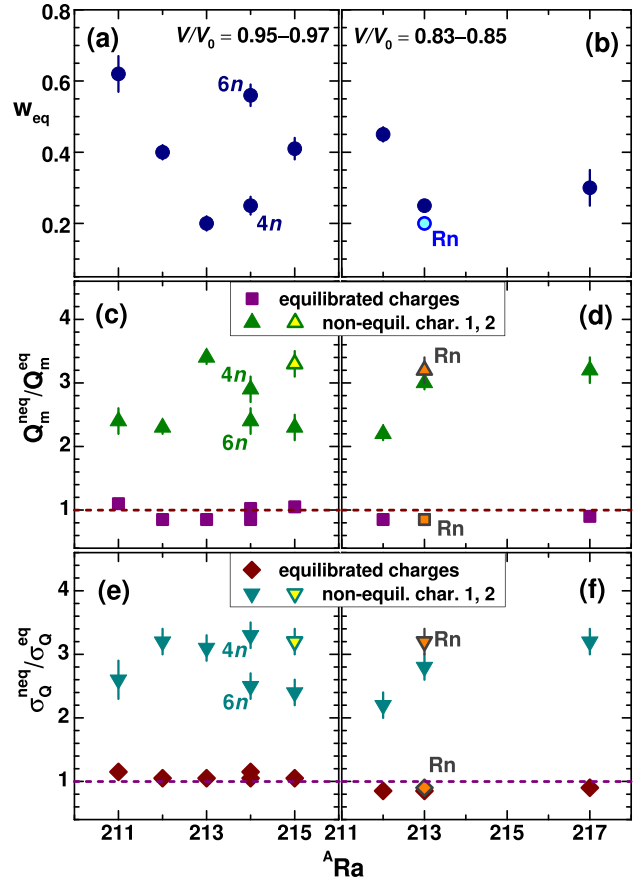

FIG. 20. (a),(b) The relative values of the equilibrated charges contribution w_{eq} to the total charge distributions as obtained with the MC simulations for Ra ERs transmitted through the deflector. (c),(d) The relative values of the mean charges for the nonequilibrated charges expressed as Q_m^{neq}/Q_m^{eq}. (e),(f) Standard deviations for the nonequilibrated charges expressed as $\sigma_Q^{neq}/\sigma_Q^{eq}$. The relative parameter data obtained in simulations for the equilibrated and nonequilibrated charges are referred to the corresponding parameter values given by the systematics [8]. Panels (a), (c), and (e) correspond to the relative velocities of Ra ERs $V/V_0 = 0.95$–0.97, whereas panels (b), (d), and (f) correspond to the relative velocities of Ra ERs $V/V_0 = 0.83$–0.85.

corresponding σ_Q^{eq} values were not corrected for the target Z. In the experiments on the study of the equilibrated charge state distribution for heavy ions of MeV energies, the carbon foils with the thicknesses from a few to tens of μg/cm^2 (depending on the heavy ion mass and energy) were used. In terms of the number of atoms, the thickness of our Pb targets are about the same and close to that of the C foil thickness of about 10 μg/cm^2. The difference between "C foil charges" and "Pb target charges" is that in the last case the equilibrium charge state distribution cannot be achieved by Ra recoils produced close to the edge of the target (downstream the beam). That means that the equilibrated charge component might be present at some level in the "observed" charge distributions for recoils produced in the reactions. In Fig. 20 the intensities or the relative values of the contribution of the equilibrated charges w_{eq} to the total charge distributions are shown (two upper

panels). The w_{eq} values vary from 0.2 to 0.6 for Ra isotopes produced in the reactions. These values are different for the same isotope produced in different evaporation channels, as in the case of ^{214}Ra produced in the $4n$ and $6n$ reactions.

Strong fluctuations obtained for w_{eq} are presumably connected to the additional ionization of the atomic inner shells of Ra recoils, which are caused by the internal conversion of nuclear transitions followed by Auger cascades. Different ways of population of the excited nuclear levels along with the different numbers of γ transitions in different Ra isotopes produced in the reactions provide for the different probabilities of the occurrence of vacancies formed in deeply-lying atomic shells as the result of nuclear transitions. These differences lead to the differences in the complementary intensities of the equilibrated and nonequilibrated charge state components.

Our attempts to systematize the parameters of the nonequilibrated charge distributions have been less successful. In Fig. 20 we show these relative values expressed as Q_m^{neq}/Q_m^{eq} and $\sigma_Q^{neq}/\sigma_Q^{eq}$ together with the values of w_{eq} for the equilibrated charges, which all together describe the observed charge distributions for Ra isotopes produced in our studies. Two sets of the data obtained at the beam energy $E_{lab} = 90$ and 69 MeV are presented in the figure, which correspond to relative velocities of the recoils $V/V_0 = 0.95$–0.97 and 0.83–0.85, respectively.

In spite of a variety of the charge parameter values, several specific features and some correlations in the data can be mentioned. Attention is drawn to some suppression in the intensities of the equilibrated component for odd Ra isotopes as compared to the same values for the neighboring even ones. This is clearly seen for the pairs of ^{212}Ra and ^{213}Ra produced in the $6n$ and $5n$ reactions, as well as for ^{214}Ra and ^{215}Ra produced in the same reactions (see Fig. 20). The difference in the intensities of the nonequilibrated charge component correlates with the Q_m^{neq} values for even-odd ERs. Thus this value for odd ^{213}Ra is about 1.5 times greater than the one corresponding to ^{212}Ra. Such relation is observed at both velocities for these recoils. The shift of the charge distribution of ^{215}Ra to higher values is reflected by the presence of the second nonequilibrated component. At the same time the data for ^{211}Ra contradict to this observation. The intensity of the equilibrated component for ^{211}Ra is about the same as for even ^{214}Ra produced in the $6n$ reaction, whereas the Q_m^{neq} and σ_Q^{neq} values are close to those of neighboring ^{212}Ra (see Fig. 20).

One can also recognize that the w_{eq} and Q_m^{neq}/Q_m^{eq} parameter values obtained for the same products, but at the different velocities of recoils, are close to each other. This occurs for ^{212}Ra and ^{213}Ra both produced in the $6n$ and $5n$ as well as in the $4n$ and $3n$ reactions (see Fig. 20). The last observation implies a similar velocity scaling for the Q_m^{neq} values as used for the equilibrated ones [8].

Attention is also drawn to the differences in the nonequilibrated charge parameters best adjusted to the measurements for ^{214}Ra produced in the $6n$ and $4n$ reactions at the same projectile energy $E_{lab} = 90$ MeV, comparing Figs. 8 and 15 (upper panel). Production of this ER in the reactions with ^{208}Pb and ^{206}Pb corresponds to about the same CN excitation energy (52.7 and 54.6 MeV, respectively). According to the HIVAP calculations [27], in the last case this energy significantly exceeds the value needed to evaporate four neutrons (the excitation function maximum is at 37 MeV), whereas in the first case, the excitation energy corresponds to the maximum of the $6n$ evaporation channel. Our estimates of the $4n$ production cross section give us the value exceeding the calculated one by a factor of 25, if we normalize the calculation to the experimental maximum for this reaction. Bearing in mind that HIVAP deals with the equilibrated decay of a CN produced in the complete fusion reaction, one may guess that in the case of ^{214}Ra produced at $E_{lab} = 90$ MeV in the $4n$ channel the main ways of its production are pre-equilibrium processes. Such high energy tailing in the xn excitation functions was earlier observed, for example, in the $^{12}C + ^{197}Au$ reaction and was assigned to the pre-equilibrium processes leading to the At isotopes production [33,34]. Therefore, the excited nuclear levels of ^{214}Ra produced in the $4n$ and $6n$ reactions at the same beam energy could be quite different that might lead to different electron emission probabilities.

B. Comparison with other data and calculations

The charge distributions of Ra recoils obtained in our study are of interest to be compared with similar ones for heavy ions at similar velocities. In Fig. 14 of Ref. [28] such comparison is shown for ^{210}Fr ($V/V_0 = 1.19$) and ^{192}Pb ($V/V_0 = 1.29$) [10]. In the latter case a magnetic spectrograph was used with the offline γ-activation technique for the detection of long-lived reaction products collected in its focal plane. The charge distributions obtained in these studies are significantly different from each other. At the same time, the transmission curves obtained for Fr ERs in [18] (Fig. 2) and in our experiments [24,28] (Fig. 4) with the electrostatic deflectors are very similar to each other. The difference in the ER charge distributions of ^{210}Fr and ^{192}Pb (leaving aside the difference in technique) can be connected with the different population of nuclear excited states of the respective compound nuclei ^{215}Fr* and ^{198}Pb*. Bearing these speculations in mind, we considered the data on the charge distributions for the recoils produced in the fusion-evaporation reactions and α decay. The latter is close to the masses of Ra recoils considered in the present work.

In Table IV we compare the charge distribution parameters for the heavy recoil ions at low velocities, which were obtained in the present study and in the earlier analysis [28] with those that we could extract from previous data [10,14] including the α-decay data [12,13]. The results of our analysis of the data [10,12–14] differ from those obtained in the original works. These results correspond to a statistically significant fit to the data in contrast to the considerations in [10,13,14] which simply preassigned several consecutive transitions with the vacancy cascades starting from holes in atomic shells. In this sense our analysis of the charge distributions is similar to our adjusting procedure used in this paper.

Thus in [13], the charge distributions of the ^{237}Np recoils resulting from the α decay of ^{241}Am with $E_\alpha = 5.486$ and 5.443 MeV ($\alpha 1$ and $\alpha 2$ in Table IV, respectively) correspond to peaks at the charges $Q^+ = 14$ (one internal conversion) and 21 (two internal conversions) for the $\alpha 1$ decay. For the $\alpha 2$ decay an additional peak at the charges $Q^+ = 26$ appears, which corresponds to three consecutive conversions. Our multi-Gaussian

TABLE IV. Mean values Q_m and standard deviations σ_Q for the equilibrated (eq) and nonequilibrated (neq) components of the recoil charge distributions studied in the present work and in [28] are compared to the results of the analysis of charge distributions for the recoils produced in the reactions [10,14] and in the α decays [12,13]. Relative velocities V/V_0 of the recoil ions, predictions for the equilibrated charge parameters according to the systematics [8], and for the mean charge as the result of a sudden vacancy in the K, L, and M atomic shells [19], which are designated as SY94 and CHK66, are also presented.

Reaction	Recoil		Experiment		SY94		Experiment				Q_m(CHK66)					
	^AZ	V/V_0	Q_m^{eq}	σ_Q^{eq}	Q_m^{eq}	σ_Q^{eq}	Q_{m1}^{neq}	σ_{Q1}^{neq}	Q_{m2}^{neq}	σ_{Q2}^{neq}	K	L_I	$L_{II,III}$	M_I	$M_{II,III}$	$M_{IV,V}$
^{4}He + ^{239}Pu	^{240}Cm[a]	0.300	1.36	3.93	1.64	0.88	19.8	6.09	32.5	8.39	11.7	13.9	11.5	12.0	11.0	10.1
^{241}Am $\xrightarrow{\alpha 1}$	^{237}Np$_1$[b]	0.125			0.51	0.50	14.1	3.40	19.9	4.28	11.5	13.7	11.3	11.7	10.7	9.7
^{241}Am $\xrightarrow{\alpha 2}$	^{237}Np$_2$[c]	0.125			0.51	0.49	13.6	3.25	20.2	4.89						
^{226}Th $\xrightarrow{\alpha 0}$	^{222}Ra$_0$[d]	0.144	1.20	0.57	0.50	0.50	4.1	1.43			11.0	13.2	10.9	11.2	10.2	9.2
^{226}Th $\xrightarrow{\alpha 1}$	^{222}Ra$_1$[e]	0.143			0.49	0.49	10.0	2.15	13.9	2.79						
^{12}C + ^{208}Pb	^{213}Rn	0.830	3.74	1.22	4.46	1.41	14.1	6.75			10.8	13.0	10.7	11.0	10.0	9.0
	^{217}Ra	0.830	4.03	1.30	4.61	1.43	14.6	6.78			11.0	13.2	10.9	11.2	10.2	9.2
	^{214}Ra	0.948	5.44	1.68	5.42	1.53	12.7	5.23								
	^{215}Ra	0.948	5.57	1.72	5.42	1.53	12.4	5.09	20.4	6.63						
^{12}C + ^{206}Pb	^{212}Ra	0.957	4.57	1.58	5.48	1.53	12.2	6.57								
	^{213}Ra	0.957	4.52	1.51	5.48	1.53	18.2	7.07								
	^{214}Ra	0.957	4.56	1.67	5.48	1.53	15.5	7.02								
^{12}C + ^{204}Pb	^{212}Ra	0.845	3.90	1.22	4.71	1.44	10.3	4.20								
	^{213}Ra	0.845	3.89	1.19	4.71	1.44	13.9	5.94								
	^{211}Ra	0.966	5.97	1.95	5.55	1.54	13.4	5.24								
^{18}O + ^{197}Au	^{210}Fr	1.19	7.56	1.86	7.05	1.70	16.4	7.12	26.7	6.65	10.9	13.1	10.8	11.1	10.1	9.1
^{16}O + ^{182}W	^{192}Pb[f]	1.29	9.29	1.13	7.51	1.75	15.3	3.64			10.5	12.6	10.4	10.5	9.6	8.5

[a]Parameter values correspond to the results of our statistically significant three-component Gauss fit to the charge distribution data presented in Fig. 5 of Ref. [14a].
[b]The same as in [a], but for the two-component Gauss fit to the data presented in Fig. 2 of Ref. [13].
[c]The same as in [b], but for the data presented in Fig. 3 of Ref. [13].
[d]The same as in [b], but for the data for the R_0 recoils presented in Fig. 2(a) of Ref. [12].
[e]The same as in [b], but for the data for the R_{111} recoils, presented in Fig. 2(b) of Ref. [12].
[f]The same as in [b], but for the data presented in Fig. 3(b) of Ref. [10].

fits to the data did not reveal a statistically significant third component in the $\alpha 2$ decay. With two-Gaussian fits to the data [13] we obtained only some redistribution in the intensity of the charge components corresponding to $W_1^{neq} = 0.52$ and $W_2^{neq} = 0.48$ for the $\alpha 1$ decay, and $W_1^{neq} = 0.3$ and $W_2^{neq} = 0.7$ for the $\alpha 2$ decay along with nearly the same values of $Q_{m1/m2}^{neq}$ and $\sigma_{Q1/Q2}^{neq}$ for both decays (Table IV). Comparing these results with those obtained for the $\alpha 0$ decay of ^{226}Th, populating the ground state of ^{222}Ra [12], we can see significant differences in the charge parameter values corresponding to one and two internal conversions, as it follows from the results of our fit to the data (Table IV). It is not the case for the intensities of both charge components for the $\alpha 1$ decay of ^{226}Th ($E_{\alpha 1} = 6.234$ MeV), corresponding to $W_1^{neq} = 0.58$ and $W_2^{neq} = 0.42$ which are close to those for the $\alpha 1$ decay of ^{241}Am (populating the 59.5 keV level of ^{237}Np). One has to mention the presence of the second charge component in the $\alpha 0$ decay of ^{226}Th ($E_{\alpha 0} = 6.337$ MeV) to the ground state of ^{222}Ra, with parameter values intermediate between those for the equilibrated and nonequilibrated charges (Table IV). These data demonstrate how the charge distribution depends on the deexcitation of the heavy recoils.

Considering the charge distribution for ^{240}Cm produced in the ^{239}Pu(^{4}He,3n) reaction [14] we could get a statistically significant fit using a three-component Gaussian function. The first component corresponds to the equilibrated charge, two others refer to the nonequilibrated charges (Table IV). This result does not contradict to the consideration presented in [14], where five consecutive converted transitions starting from holes in the L_{II}, L_{III} shells and leading to the average charges $Q^+ \approx 12$, 19, 24, 29, and 33 were obtained as the result of the corresponding analysis.

The results obtained in this work [14] along with the predictions of the mean charges as the result of a sudden vacancy in the K, L, and M atomic shells [19] can be compared to the results of our analysis of the charge distributions obtained for Ra recoils produced in the ^{12}C + Pb reactions. For the most of Ra recoils the mean charge value of the nonequilibrated component lies in the range between 12 and 15. These values are close to the mean charge resulted in a sudden vacancy in the L atomic shells [19] (see Table IV). In the case of ^{215}Ra produced in the ^{208}Pb(^{12}C,5n) reaction, a second nonequilibrated component was added to describe the transmission curve. The mean charge of this component is comparable with the mean charges observed after two internal conversions [13,14] (see Figs. 7 and 8 and Table IV). Along with this observation, the large values of the mean charge and standard deviation obtained for ^{213}Ra produced in the ^{206}Pb(^{12}C,5n) reaction (see

Table IV) might be an indication of the presence of a second component in the nonequilibrated charge distribution. It was not resolved in our adjusting procedure. One has to mention relatively large absolute values of the mean charge and width for both components of the nonequilibrated charges of ^{210}Fr produced in the ^{197}Au(^{18}O,5n) reaction [28] (see Table IV). These values are higher than those that characterize the charge distributions resulting from one and two converted transitions observed for low velocity heavy recoils [12–14] (see Table IV). These differences might be the result of the general mean charges dependance as a function of the HI velocity [16].

Our analysis of the measured transmission (yield) curves did not reveal the second component of the nonequilibrated charges, which was manifested in several cases (for ^{215}Ra, ^{213}Ra, ^{210}Fr, and, probably, for ^{211}Ra). The reason might be a small transmission efficiency of the deflector for HIs with a low electric rigidity (low energy Ra recoils with very high ionic charges correspond to such species). To check this assumption, the transmission was simulated for ^{215}Ra having a uniform charge distribution (UCD) over the range from $Q_i^+ = 1$ to 88 assuming the same energy distribution as was used in the description of the measured transmission curve (Fig. 7). In such a manner the contour map of the transmission values as a function of the ionic charge and electric field strength could be obtained. This contour map is shown in Fig. 21(a) together with the curve for the ^{215}Ra transmission efficiency integrated over the charges that could be transmitted through the deflector [Fig. 21(b)]. As we can see, one can expect the highest transmission efficiency at $U = 0.1$–0.5 kV/cm that corresponds to the maxima at charge states with $Q_i^+ = 21$–82 [local maxima in the contour map is the result of finite steps in the U variation as indicated in Fig. 21(b)]. In our cases a second maximum corresponding to the nonequilibrated charges in the measured transmission curves is observed at $U = 0.5$–1.0 kV/cm. At these field strengthes Ra ions with $Q_i^+ > 20$ could be transmitted with the essentially reduced efficiencies, as one can see in Fig. 21(a). Thus, the local maximum in the transmission efficiency at $U_m \sim 0.5$ kV/cm corresponds to the value of $Q_m^+ \sim 21$, whereas at $U_m \sim 1.0$ kV/cm it is shifted to $Q_m^+ \sim 11$. Along with this shift the width of the transmitted charge distribution is essentially reduced in going from $U = 0.5$ to 1.0 kV/cm. As a consequence, Ra ions with rather high charges could not effectively be transmitted through the deflector at $U =$ 0.5–1.0 kV/cm. These charges correspond to the "tails" of the nonequilibrated charge distributions, as it follows from our simulations using multi-Gaussian approach to the description of the ionic charges. So, one may conclude that more precise measurements with higher sensitivity at small electric field strengths are desired to obtain the total spectrum of the ionic charges for Ra recoils produced in the ^{12}C + Pb reactions.

VI. SUMMARY AND CONCLUSION

The ionic charge distributions for heavy fusion-evaporation reaction products or evaporation residues (ERs) are of interest from various points of view. Fragmentary data on the ionic charges were earlier obtained for ERs of rare-earth elements, some isotopes of Pb and Po [10,11,15,16], as well as for low-energy heavy actinides [14]. The data show very broad charge distributions and imply the presence of the equilibrated (relatively low) and nonequilibrated (relatively high) charges [10,14–16] in the distributions. The latter are treated as the result of the additional ionization of inner atomic shells, which is caused by the internal conversion of nuclear transitions followed by the Auger cascades [2,10,14,16]. In this regard, very high charge states are interpreted as the result of several consecutive internal conversions accompanying by the Auger cascades starting from the holes in the inner shells [10,14].

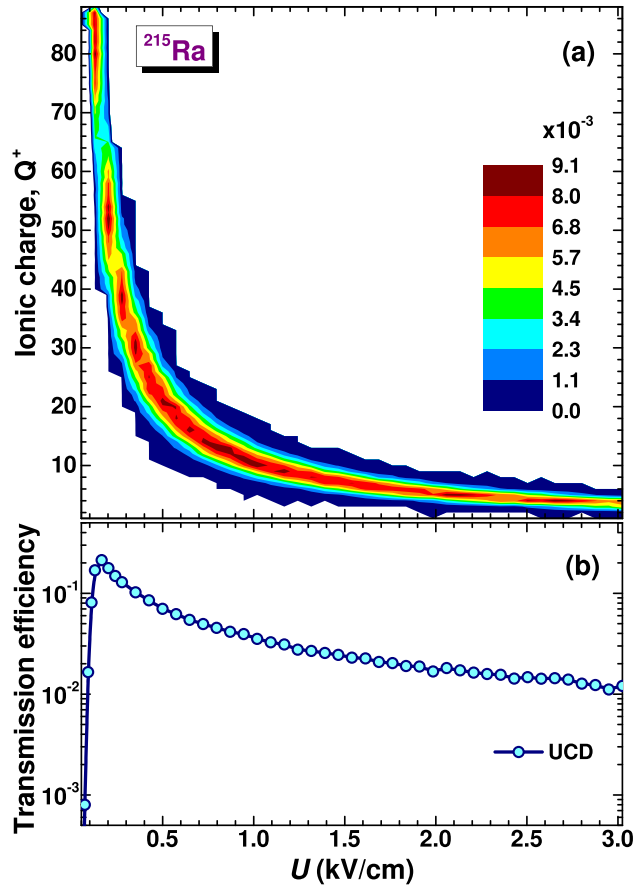

FIG. 21. (a) Contour map of the transmission efficiency values for ^{215}Ra simulated with a uniform charge distribution (UCD) as a function of the ionic charge and electric field strength. (b) The transmission efficiency curve for ^{215}Ra, which was obtained with the integration over uniform charges transmitted through the deflector [shown in panel (a)] as a function of the electric field strength.

The ionic charge distribution for Ra ERs produced in the Pb(^{12}C,xn) fusion-evaporation reactions were studied in the present work. The data were obtained with the measurements of the transmission efficiency (yield) for ERs as a function of the electric field strength of the electrostatic deflector [23] used in the experiments. Two-humped transmission (yield) curves obtained for all Ra isotopes produced in the reactions were described with the Monte Carlo simulations of their charge and energy used for trajectory calculations through the deflector. Since the ER energy can be reasonably calculated taking into account evaporation of neutrons from compound nuclei and stopping of ERs inside the target [28], the description of

the transmission (yield) curves could be performed solely by adjusting the ER charges.

The parameter values for the equilibrated charge distribution $Q_{\mathrm{m}}^{\mathrm{eq}}$ (mean charge) and $\sigma_{\mathrm{Q}}^{\mathrm{eq}}$ (standard deviation) given by systematics [8] were scaled to obtain corresponding values for the equilibrated and non-equilibrated charge components. The values of the mean charge and standard deviation obtained for the equilibrated charges of Ra isotopes turned out to be close to the values predicted by this systematics. The corresponding values $Q_{\mathrm{m}}^{\mathrm{neq}}$ and $\sigma_{\mathrm{Q}}^{\mathrm{neq}}$ for the nonequilibrated charge component appeared to be two to three times greater than the same predictions. Furthermore, in contrast to the equilibrated charges, the parameters of the nonequilibrated charge distributions have widely scattered values that does not allow us to systematize them. At the same time, the majority of the mean charge values for the nonequilibrated distributions are close to the corresponding values for the ^{237}Np recoils resulting from the α decay of ^{241}Am [13] and for the ^{240}Cm recoils produced in the ^{239}Pu(^{4}He,$3n$) reaction [14]. Those components were interpreted as the result of the conversions of the γ transitions from the excited level of the actinide nuclei. For ^{215}Ra and ^{210}Fr we could extract a second component from the nonequilibrated part of the charge distributions. The corresponding $Q_{\mathrm{m2}}^{\mathrm{neq}}$ values for their charge distributions are also close to the similar values derived for the ^{237}Np and ^{240}Cm recoils [13,14]. The corresponding components of the charge distributions were interpreted as the result of two consecutive conversions for the actinide nuclei. The observation of higher charges corresponding to the larger number of the consecutive conversions for Ra recoils requires the measurements with higher sensitivity at small electric field strengthes of the deflector.

The results of the present study are in agreement with earlier measurements of the ionic charge distributions observed for heavy recoils produced in fusion-evaporation reactions and resulting from α decay. Very broad charge spectra are inherent in such recoils, as found in a number of experiments. The charge distributions obtained in the present work for Ra recoils produced in the Pb(^{12}C,xn) reactions allow us to derive unambiguously the equilibrated and nonequilibrated components from the measured data. The parameter values of the equilibrated charge distributions are close to those predicted by the different systematics considering the heavy ion equilibrated charges. At the same time, the parameter values for the nonequilibrated components are specific for particular Ra isotopes, although the mean charges have about the same value in the most cases. The relative intensities of the nonequilibrated components fluctuates from an isotope to isotope. These differences, as well as some differences in the parameter values, are the results of the internal conversion of specific nuclear transitions inherent in each Ra isotopes along with the different ways of population of these nuclear states in the reactions.

Theoretical considerations of these processes are of interest from the point of view of getting the quantitative description of the ionic charge distributions of heavy recoils produced in nuclear reactions. Such description, in particular, will be useful in experiments with the electromagnetic separators intended for the study of the heavy nucleus recoils produced in the reactions induced by the accelerated heavy ions.

ACKNOWLEDGMENTS

We wish to thank the XTU Tandem staff for their careful work and our colleagues Dr. B. R. Behera, Dr. A. Gadea, Dr. A. Latina, Dr. S. Beghini, and Dr. M. Trotta, who took part in some beam experiments.

[1] H.-D. Betz, Rev. Mod. Phys. **44**, 465 (1972).
[2] N. K. Skobelev, Fiz. Elem. Chastits At. Yadra **20**, 1439 (1989) [Sov. J. Part. Nucl. **20**, 613 (1989)].
[3] V. S. Nikolaev and I. S. Dmitriev, Phys. Lett. A **28**, 277 (1968).
[4] R. O. Sayer, Rev. Phys. Appl. **12**, 1543 (1977).
[5] Y. Baudinet-Robinet, H. P. Garnir, and P. D. Dumont, Phys. Lett. A **63**, 19 (1977); Y. Baudinet-Robinet, Nucl. Instrum. Methods Phys. Res. **190**, 197 (1981); Phys. Rev. A **26**, 62 (1982).
[6] K. Shima, T. Ishihara, and T. Mikumo, Nucl. Instrum. Methods Phys. Res. **200**, 605 (1982).
[7] K. Shima, N. Kuno, M. Yamanouchi, and H. Tawara, At. Data Nucl. Data Tables **51**, 173 (1992).
[8] R. N. Sagaidak and A. V. Yeremin, Nucl. Instrum. Methods Phys. Res. B **93**, 103 (1994).
[9] G. Schiwietz and P. L. Grande, Nucl. Instrum. Methods Phys. Res. B **175–177**, 125 (2001).
[10] V. Z. Maidikov, N. T. Surovitskaya, N. K. Skobelev, and O. F. Nemetz, Yad. Fiz. **36**, 1103 (1982) [Sov. J. Nucl. Phys. **36**, 645 (1982)].
[11] N. H. Steiger, in *Proceedings of the III Conference on Reactions between Complex Nuclei, Asilomar, USA, 1963*, edited by A. Ghiorso (University of California Press, Berkeley, 1963), p. 407.
[12] K. Gunter, F. Asaro, and A. C. Helmholz, Phys. Rev. Lett. **16**, 362 (1966).
[13] W. De Wieclawik, C. R. Acad. Sci. Ser. B **266**, 577 (1968).
[14] V. Metag, D. Habs, H.-J. Specht, G. Ulfert, and C. Kozhuharov, Hyperfine Interact. **1**, 405 (1976); D. Habs, V. Metag, H.-J. Specht, and G. Ulfert, Phys. Rev. Lett. **38**, 387 (1977); G. Ulfert, D. Habs, V. Metag, and H.-J. Specht, Nucl. Instrum. Methods Phys. Res. **148**, 369 (1978).
[15] N. K. Skobelev, V. Z. Maidikov, G. S. Popeko, Yu. V. Gofman, O. F. Nemetz, and Yu. Ts. Oganessian, Yad. Fiz. **29**, 316 (1979) [Sov. J. Nucl. Phys. **29**, 615 (1979)].
[16] N. K. Skobelev, V. Z. Maidikov, and N. T. Surovitskaya, Z. Phys. A **314**, 5 (1983).
[17] W. Bonin, M. Dahlinger, S. Glienke, M. Krämer, D. Habs, B. Schwartz, and H. Backe, Z. Phys. A **310**, 249 (1983); M. Dahlinger, W. Bonin, E. Kankeleit, and H. Backe, Nucl. Instrum. Methods Phys. Res. **219**, 513 (1984).
[18] K.-T. Brinkmann, A. L. Caraley, B. J. Fineman, N. Gan, J. Velkovska, and R. L. McGrath, Phys. Rev. C **50**, 309 (1994).
[19] T. H. Carlson, W. E. Hunt, and M. O. Krause, Phys. Rev. **151**, 41 (1966).

[20] A. M. El-Shemi, Turk. J. Phys. **28**, 229 (2004); A. M. El-Shemi and Y. A. Lotfy, Eur. Phys. J. D **32**, 277 (2005).
[21] R. N. Sagaidak, G. N. Kniajeva, I. M. Itkis, M. G. Itkis, N. A. Kondratiev, E. M. Kozulin, I. V. Pokrovsky, A. I. Svirikhin, V. M. Voskressensky, A. V. Yeremin, L. Corradi, A. Gadea, A. Latina, A. M. Stefanini, S. Szilner, M. Trotta, A. M. Vinodkumar, S. Beghini, G. Montagnoli, F. Scarlassara, D. Ackermann, F. Hanappe, N. Rowley, and L. Stuttgé, Phys. Rev. C **68**, 014603 (2003).
[22] L. Corradi, B. R. Behera, E. Fioretto, A. Gadea, A. Latina, A. M. Stefanini, S. Szilner, M. Trotta, Y. Wu, S. Beghini, G. Montagnoli, F. Scarlassara, R. N. Sagaidak, S. N. Atutov, B. Mai, G. Stancari, L. Tomassetti, E. Mariotti, A. Khanbekyan, and S. Veronesi, Phys. Rev. C **71**, 014609 (2005).
[23] S. Beghini, C. Signorini, S. Lunardi, M. Morando, G. Fortuna, A. M. Stefanini, W. Meczynski, and R. Pengo, Nucl. Instrum. Methods Phys. Res. A **239**, 585 (1985).
[24] R. N. Sagaidak, L. Corradi, B. R. Behera, E. Fioretto, A. Gadea, A. Latina, A. M. Stefanini, S. Szilner, S. Beghini, G. Montagnoli, F. Scarlassara, and M. Trotta, LNL Annual Report 2004, INFN-LNL(REP)204/2005, Legnaro, 2005, p. 37.
[25] R. N. Sagaidak, N. A. Kondratiev, L. Corradi, E. Fioretto, T. Mijatović, A. M. Stefanini, G. Montagnoli, and F. Scarlassara, LNL Annual Report 2014, INFN-LNL Report 241, Legnaro, 2015, pp. 58, 60.
[26] http://www.nndc.bnl.gov/nudat2/indx_dec.jsp.
[27] W. Reisdorf, Z. Phys. A **300**, 227 (1981); W. Reisdorf and M. Schädel, *ibid.* **343**, 47 (1992).
[28] R. N. Sagaidak, V. K. Utyonkov, and F. Scarlassara, Nucl. Instrum. Methods Phys. Res. A **700**, 111 (2013).
[29] J. F. Ziegler, code SRIM-2013, http://www.srim.org.
[30] R. N. Sagaidak and A. N. Andreyev, Phys. Rev. C **79**, 054613 (2009).
[31] R. Bimbot, D. Gardes, and M. F. Rivet, Nucl. Phys. A **189**, 193 (1972).
[32] T. Nomura, K. Hiruta, M. Yoshie, and O. Hashimoto, Phys. Rev. C **9**, 1168 (1974).
[33] J. D. Stickler and K. J. Hofstetter, Phys. Rev. C **9**, 1064 (1974); K. J. Hofstetter and J. D. Stickler, *ibid.* **9**, 1072 (1974).
[34] P. Vergani, E. Gadioli, E. Vaciago, E. Fabrici, E. Gadioli Erba, M. Galmarini, G. Ciavola, and C. Marchetta, Phys. Rev. C **48**, 1815 (1993).